Title

Hydrogen Bonding Controls the Structural Evolution in Perovskite-Related Hybrid Platinum(IV) Iodides

Journal

Inorganic Chemistry, 57(16)

ISSN

0020-1669 1520-510X

Authors

Evans, Hayden A
Fabini, Douglas H
Andrews, Jessica L
et al.

Publication Date

2018-08-03

DOI

10.1021/acs.inorgchem.8b01597

Peer reviewed

Hydrogen Bonding Controls Structural Evolution in Perovskite-Related Hybrid Platinum (IV) Iodides

Hayden A. Evans,[†,‡] Douglas H. Fabini,[¶,‡] Jessica L. Andrews,[†] Mitchell Koerner,[§] Molleigh B. Preefer,[†,‡] Guang Wu,[†] Fred Wudl,[¶] Anthony K. Cheetham,[‡,‖] and Ram Seshadri[*,†,¶,‡]

†*Department of Chemistry and Biochemistry*
University of California, Santa Barbara, California 93106, United States
‡*Materials Research Laboratory*
University of California, Santa Barbara, California 93106, United States
¶*Materials Department*
University of California, Santa Barbara, California 93106, United States
§*Physics Program, College of Creative Studies*
University of California, Santa Barbara, California 93106, United States
‖*Department of Materials Science and Engineering*
National University of Singapore, Singapore 117575.

E-mail: seshadri@mrl.ucsb.edu

Abstract

We describe solid-state structural evolution in four hybrid hexaiodoplatinate(IV) compounds, demonstrating the increasingly important role that extended hydrogen bonding plays in directing the structure across the series. The compounds are A_2PtI_6, where *A* is one of the following amines: ammonium, NH_4^+; methylammonium MA, $CH_3NH_3^+$; formamidinium FA, $CH_2(NH_2)_2^+$; and guanidinium GUA, $C(NH_2)_3^+$, and are closely related in structure and properties to the hybrid halide perovskites of Pb(II) that have recently established their prowess in optoelectronics. The first three of these compounds crystallize in the vacancy-ordered double perovskite $A_2Pt\square I_6$ ($\square$ indicates a vacant site) structure in the K_2PtCl_6 archetype, despite the relatively large perovskite tolerance factors involved. The last compound, $(GUA)_2PtI_6$ crystallizes in a vacancy-ordered variant of the hexagonal $CsNiCl_3$ structure: the K_2MnF_6 structure. A combination of ^{195}Pt and ^{1}H solid-state NMR spectroscopy and detailed density functional theory calculations help to reveal structural trends and establish the hydrogen-bonding tendencies. The calculations and measured optical properties support the surprising observation in these iodosalt compounds that for smaller *A* cations, the conduction bands are considerably disperse, despite lacking extended I–Pt–I connectivity.

Introduction

The AMX_3 perovskite crystal structure is unique in that it is the simplest and only ternary structure type that has near-180° extended *M*–*X*–*M* interactions in all three dimensions. The extended interactions result in the disperse bands that can enable a host of interesting functional properties in perovskites. Halide perovskites with the formula AMX_3, where *A* is an alkali metal or small organic cation, *M* is a divalent main group metal, and *X* are halides are one such materials family combining impressive optoelectronic properties with remarkable ease of preparation.[1–4] Thin film, single junction photovoltaic devices of these perovskite materials have exhibited upwards of 22 % power conversion efficiency (PCE), owing to a direct band gap electronic structure, inherently long lived charge carriers, and high defect tolerance of the perovskite active material.[5]

Halide perovskites, like their oxide counterparts, are a diverse class of materials that can tolerate many different kinds of chemical substitutions.[6,7] This includes *A*-site substitution by different ions to obtain layered variants.[8,9] The substitution of divalent *M* by a trivalent ion such as Bi(III) can result in a vacancy-ordered perovskite such as $K_3Bi_2\square I_9$ where every third *M* is missing, indicated by a vacancy □.[10] Forking the charge on the divalent *M*-site through substitution with mono- and trivalent cations results in double-perovskites or elpasolites.[11–15] Finally, substitution on the *M* site with a tetravalent ion creates vacancy-ordered perovskites where *M* atoms and vacancies □ (usually) display 3D rock-salt like ordering. The aristotype for this structure type is K_2PtCl_6 in the $Fm\bar{3}m$ space group.[16] It is interesting to note that vacancy-ordered perovskites are rare or non-existent in the oxide perovskite world, even when permitted by the perovskite tolerance factor (for example, the hypothetical compound $La_2W\square O_6$), as a consequence of the cost of oxide-oxide repulsions and of stabilizing high cation charge states in isolated species.

Halide compounds with the K_2PtCl_6 composition have been known for a long time. They have been examined as diamagnetic hosts (A_2PtI_6) of paramagnetic ions (Ir^{4+}, Re^{4+}, Os^{4+}),[17] and have been studied for their interesting lattice dynamics associated with free

rotation of isolated MX_6 octahedra.[18] A comprehensive review by Armstrong on A_2MX_6 materials (A = NH_4, K, Rb, Cs, M= Pt, Ir, Os, Re, W, and X = Cl, Br, I) provides an overview.[17] The structure type is also associated with charge disproportionation of the M site metal, as seen for Cs_2SbCl_6, which displays mixed-valence Sb(III) and Sb(V) atoms instead of what would appear to be Sb(IV).[19] Hybrid A_2MCl_6 and A_2MBr_6 compounds were previously studied for how organic cations, predominantly methylammonium in $(MA)_2MX_6$ compounds (M= Sn, Pt, Te and X = Cl, Br, I)[20–24] or dimethylammonium in $(DMA)_2MX_6$ compounds (M= Sn, Pt, Te, Se and X = Cl, Br),[25–27] impact structural phase transitions through molecular reorientation.

The 2014 demonstration that the molecular iodostannate salt Cs_2SnI_6 is an effective hole conductor — despite not possessing extended I–Sn–I connectivity — that can be employed as the hole-transport layer in dye-sensitized solar cells has been an important landmark in the way in which these materials are viewed.[28] Related work that has appeared includes a study of the role of defects in determining the properties of Cs_2SnI_6 and Cs_2TeI_6[29] and of the role of anharmonicity in dictating the properties of A_2SnI_6 when A = CH_3NH_3 or $CH(NH_2)_2$.[31]

In the present work, we study the series of compounds A_2PtI_6 series [A = ammonium (NH_4^+), methylammonium [$CH_3NH_3^+$ abbreviated MA], formamidinium [$CH(NH_2)_2^+$ abbreviated FA], and guanidinium [$C(NH_2)_3^+$ abbreviated (GUA)]. The synthesis and composition of several A_2PtI_6 compounds were already reported by Datta in 1913,[32] albeit with no descriptions of the structure. Furthermore, Datta refers back to some literature on these from the first half of the 19th century. The crystal structures of A_2PtI_6 at room temperature for A = NH_4[33,34] and MA[20] have been previously reported. We demonstrate that hydrogen bonding becomes especially important in retaining the vacancy-ordered perovskite in the compounds with the larger A cations. Specifically, if the organic cation is small, I–I van der Waals interactions guide atomic packing, and if the organic cation is large, hydrogen bonding forces (N–H$\cdots$I) guide the structure. Consequences of the hydrogen bonding

tendencies manifest in solid-state ^{1}H NMR experiments and in density functional theory (DFT) based electronic structure calculations. Just as in the case of Cs_2SnI_6,[28] we find that for the smaller *A* cations, the valence and conduction bands of A_2PtI_6 display surprisingly disperse electronic bands. The measured optical properties are compared with the results of DFT calculations.

Experimental

The starting material CH_3NH_3I was prepared by adding a solution of CH_3NH_2 (1.00 eq. 33% wt/wt in absolute ethanol, Spectrum) solution of HI (1.05 eq., 57% wt/wt in aqueous solution, Spectrum) held at 0 °C. After stirring for 2 h at 0 °C, excess solvent was removed using a rotary evaporator. The precipitate was recrystallized twice from a hot ethanol/water mixture, washed with ether, and dried under vacuum overnight to give white crystals with a plate-like habit.

$CH(NH_2)_2I$, FAI was prepared by metathesis, by adding solid formamidinium acetate (1.00 eq, 99%, Sigma-Aldrich) to room temperature HI (2.0 eq., 57% wt/wt in aqueous solution, Spectrum.) After stirring for 2 h, excess solvent was removed using a rotary evaporator. The residue was washed with boiling toluene to remove any potential triazine contaminant, recrystallized from ethanol, vacuum filtered, and dried to give white crystals with a needle-like habit.

$(NH_4)_2PtI_6$ was prepared by combining 0.46 mg NH_4I (0.300 mmol, Sigma Aldrich, 99.5%) and 22.64 mg (0.150 mmol) $PtCl_2$ (Strem, 99.9%) in 6.0 g 57% wt/wt HI, which was brought to gentle reflux for 15 min. The solution was slowly cooled to room temperature and placed in a refrigerator overnight. The solution was vacuum filtered cold and washed with diethyl ether. The isolated crystals were vacuum-dried overnight. Small, dark-bronze cubic habit crystals were isolated. The hydroiodic acid used for this and all other iodoplatinate reactions did not contain the reducing stabilizer hypophosphorous

acid. The iodine contained in solution (due to not using the reducing stabilizer) is thought to be responsible for the oxidation of Pt^{2+} to Pt^{4+}.

$(MA)_2PtI_6$ was prepared by combining 0.717 mg CH_3NH_3I (0.300 mmol) to 60 mg (0.150 mmol) $PtCl_2$ (Strem, 99.9%,) in 9.3 g 57% wt/wt hydroiodic acid. This solution was brought to gentle reflux or 25 min., slowly cooled to room temperature, and placed in freezer overnight. This solution was vacuum filtered cold and washed with diethyl ether. Isolated crystals were vacuum-dried overnight. Dark-bronze colored, hexagonal plate habit crystals were isolated.

$(FA)_2PtI_6$ was prepared by combining 130 mg (0.760 mmol) $CH(NH_2)_2I$ with 100 mg (0.375 mmol) of $PtCl_2$ (Strem, 99.9%) in 15.5 g of 57% wt/wt hydroiodic acid. This solution was brought to a temperature no greater than 70°C, and stirred for 25 min. The solution was slowly cooled to room temperature (no precipitate forms at this point) and placed in a freezer overnight. Bronze, metallic-looking needles of $(FA)_2PtI_6$ were vacuum filtered cold, washed with diethyl ether, and vacuum dried overnight. Exceeding 70°C results in degradation of the FA cation, producing free ammonium.

$(GUA)_2PtI_6$ was prepared by combining 282 mg $C(NH_2)_3I$ (1.5 mmol (Sigma Aldrich) and 200 mg (0.75 mmol) $PtCl_2$ (Strem, 99.9%,) in 15.5 g 57% wt/wt hydroiodic acid. The solution temperature was raised to gentle reflux for 25 min., slowly cooled to room temperature, and placed overnight in a freezer. This solution was vacuum-filtered cold and washed with diethyl ether. The isolated crystals were vacuum-dried overnight. Large, dark grey, block habit crystals were isolated. We note that if a more concentrated reaction mixture is employed, an unidentified Pt-containing contaminant co-forms with the desired compound. Careful control of concentration allows the pure compounds to be obtained.

Single crystal X-ray diffraction data was collected on a Bruker KAPPA APEX II diffractometer equipped with an APEX II CCD detector using a TRIUMPH monochromator with a Mo Kα X-ray source (λ = 0.71073 Å). The crystals were mounted on a cryoloop under Paratone-N oil and kept under nitrogen. Absorption correction of the data was carried out

using the multiscan method as implemented in SADABS.[35] Subsequent calculations were carried out using SHELXTL.[36] Structure determination was done using intrinsic methods. All hydrogen atom positions were omitted. Structure solution, refinement, and creation of publication data was performed using SHELXTL. Crystal structures were visualized using the VESTA software suite.[37]

Powder X-ray diffraction was performed on a Panalytical Empyrean Powder Diffractometer (Bragg-Brentano HD module, no monochromator) equipped with a Cu source λ = 1.5418 Å. Rietveld refinements were performed in the TOPAS software suite.[38] Solid state NMR: ^{1}H and ^{195}Pt single-pulse experiments, ^{1}H inversion recovery experiments, and ^{14}N spin echo experiments were conducted on a 500 MHz (11.7 T) Bruker Avance NMR spectrometer with a Bruker 4 mm H/X/Y triple resonance MAS probe. Powdered samples were packed into a 4 mm zirconia MAS rotor and capped with a Kel-F drive cap. ^{1}H chemical shift was referenced to adamantane (1.71 ppm relative to TMS at 0 ppm). ^{195}Pt chemical shift was referenced to a 1 M solution of Na_2PtCl_6 in D_2O (0 ppm). Longitudinal relaxation (T_1) experiments utilized the inversion recovery method. CSA parameters for ^{195}Pt were extracted using the SOLA line shape analysis module within Bruker Topspin. Solid state UV-vis spectra were obtained using an integrating sphere equipped Shimadzu UV3600 UV-NIR Spectrometer in diffuse reflectance mode. The title compounds tested were suspended in $BaSO_4$ medium (*via* grinding). The reflectance spectra were Kubelka-Munk transformed for relative absorbance spectra. Thermogravimetric analysis (TGA) on all compounds was conducted using a TA Instruments Discovery instrument. A rate of 25 cm^3/min dry nitrogen purge was employed with a temperature ramp rate of 10°C/min. The maximum temperature of the experiment was 900°C. Differential scanning calorimetry (DSC) measurements were performed using a TA Q2000 calorimeter. Samples (2 mg to 10 mg each) were hermetically sealed inside TZero aluminum pans. Samples were first cooled to −150°C, then heated to most 180°C at 10 °C/min. This was repeated for three cycles.

Ab initio calculations of the crystal structures, electronic structures, and optical properties were performed with the Vienna *Ab initio* Simulation Package (VASP)[39–42] which implements the Kohn-Sham formulation of density functional theory (DFT) using a plane wave basis set in conjunction with projector augmented waves.[43,44] The generalized gradient approximation was employed using the exchange and correlation functional of Perdew, Burke, and Ernzerhof (GGA-PBE).[45] The plane wave basis set cutoff energy (800 eV) and k-point mesh density (≈1500 k-points per reciprocal atom for convergence of the charge density, ≈40,000 k-points *per* reciprocal atom for computing the density of states and dielectric function, all Γ-centered Monkhorst-Pack sampling[46] were chosen based on convergence of the total energy.) Structure relaxations were performed, including van der Waals corrections (DFT-D3 method of Grimme),[47] to a force tolerance of 4 meV Å^{-1}. All relaxed structures preserved the original space group symmetry, with the exception of $(MA)_2PtI_6$, which appeared to drift slightly from the original $R\bar{3}m$ high symmetry space group symmetry, but that was found within a 0.001 Å lattice parameter tolerance using the FINDSYM program[48] to actually retain $R\bar{3}m$. This symmetrized cell was used for subsequent calculations to minimize computational expense. Brillouin zone paths for band structure calculations were taken from Setyawan and Curtarolo.[49] Frequency-dependent dielectric functions were calculated using the method described by Gajdoš *et al.*, as implemented in VASP.[50] The dielectric tensors were converted to isotropic equivalents, and subsequently to isotropic absorption coefficients via custom python code. Band structures and densities of states, including orbital projections, were visualized using custom python code.

Results and Discussion

All the samples were prepared by standard methods (precipitation from acid) and their structures solved by single crystal X-ray diffraction; details of the methods employed are

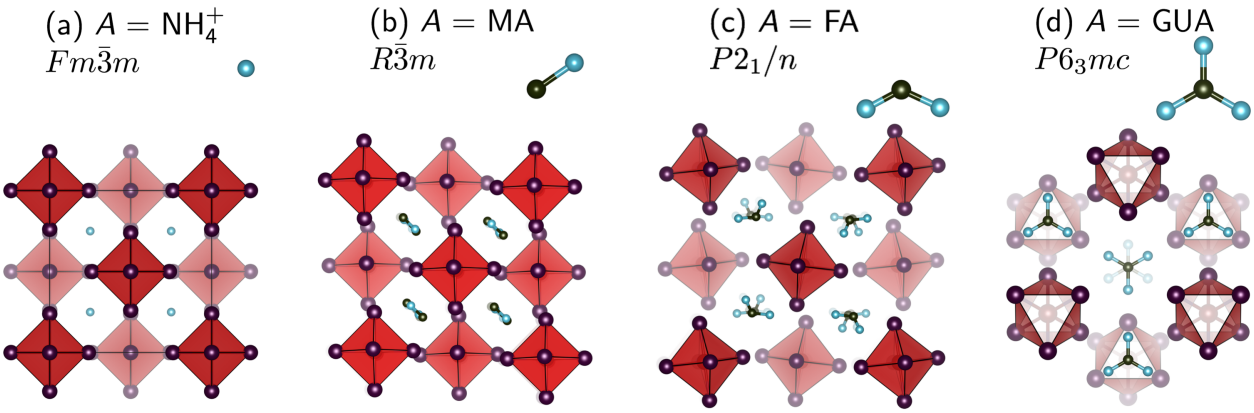

Figure 1: Crystal structure evolution at room temperature of the title compounds (a) $(NH_4)_2PtI_6$, (b) $(MA)_2PtI_6$, (c) $(FA)_2PtI_6$, (d) $(GUA)_2PtI_6$ displaying the evolution from a cubic to distorted K_2PtI_6 type to eventually, the hexagonal, polar K_2MnF_6 structure type. The shading of the $[PtI_6]^{2-}$ octahedra reflects depth perpendicular to the display plane. The $(NH_4)_2PtI_6$, $(MA)_2PtI_6$, and $(FA)_2PtI_6$ are viewed as if looking down [001] of the cubic parent.

provided in the Experimental section above. Figure 1 depicts the A_2PtI_6 series beginning with the smallest organic cation containing compound, $(NH_4)_2PtI_6$, and ending with the largest, $(GUA)_2PtI_6$. The $A = NH_4^+$ compound crystallizes in undistorted cubic K_2PtCl_6 structure (space group $Fm\bar{3}m$), the MA compound in a rhombohedrally distorted variant structure (space group $R\bar{3}m$), the (FA) compound in a monoclinic variant (space group $P2_1/n$). The A = GUA compound crystallizes in a distinct structure type, of K_2MnF_6 in the polar space group $P6_3mc$.[51] All compounds could be prepared as pure powders as confirmed by Rietveld refinement of powder X-ray diffraction data (fits displayed in the Supporting Information).

The panels of Figure 2 display the evolution with effective ionic radius of (a) the volume *per* formula unit and (b) the perovskite tolerance factor for the A_2PtI_6 compounds reported here, and data on all-inorganic Rb_2PtI_6 and Cs_2PtI_6.[34] The effective radii employed for Rb^+ and Cs^+ are the 12-coordinate Shannon values.[52,53] Values for other A cations are from Kieslich, Sun, and Cheetham.[54] Six-coordinate radii were employed because these appear to be consistent with the methods employed to estimate the radii of the more complex ions.

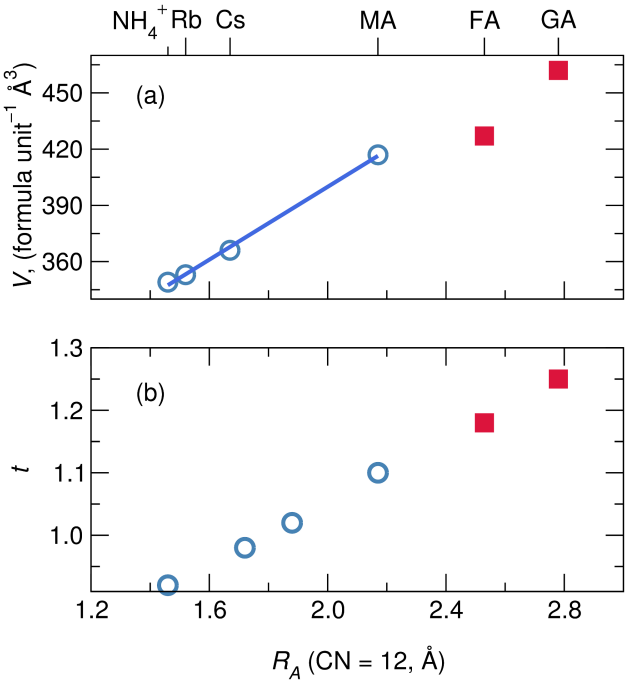

Figure 2: Evolution of (a) volumes *per* formula unit and (b) the perovskite tolerance factors, as a function of the *A*-effective ionic radius for octahedral coordination (CN = 12). Radii values employed are from Kieslich, Sun, and Cheetham[54] (for NH_4^+, MA, FA, and GUA) and from Shannon[52,53] for Rb^+ and Cs^+. The symbols for A = MA and GUA are distinct to indicate they do not follow the same volume/size trend as the other compounds.

Panel (a) of Figure 2 shows that all of the compounds except for A = FA and GUA follow a simple trend that suggests the volume *per* formula unit of A_2PtI_6 depends solely on the A-cation separating out the molecular $[PtI_6]^{2-}$ octahedra in the solid state. The A = FA and GUA compounds do not follow this trend, pointing to a distinct structural role, which we will presently implicate with hydrogen bonding tendencies. Panel (b) displays the evolution of the tolerance factors t of these compounds. While the tolerance factor is frequently employed to understand perovskites, including ones with more complex ammonium cations,[54] its utility in vacancy-ordered compounds of the K_2PtCl_6-type has been recently noted.[55] We observe that the A = MA and FA compounds have tolerance factors that are well in excess of the range usually expected for compounds with perovskite-like arrangements of their octahedra. The other surprise is that the $(FA)_2PtI_6$ appears to display tilting and rotation, which is contrary to the expectation for $t > 1$. While t should be interpreted with care because of the absence of extended I–Pt–I connectivity in the structure, it appears to be insightful here. In particular, when t is significantly greater than unity, we see the kind of structural transformation, from $Fm\bar{3}m$ K_2PtCl_6-type, to $P6_3mc$ K_2MnF_6-type that is reminiscent of what happens with perovskites when the tolerance factor becomes large, for example, the transformation from the structure of $SrRuO_3$ to $BaRuO_3$.[56]

To complement the crystallography and to better understand the role of the A-cation, we have employed room temperature ^1H and ^{195}Pt solid state nuclear magnetic resonance (ssNMR) spectroscopy. ^1H ssNMR confirmed the identity of each molecular cation and probed aspects of each cations motion, and ^{195}Pt ssNMR examined the local Pt environments to confirm our crystallographic models. ^{195}Pt single-pulse NMR spectra with 10 kHz magic-angle spinning (MAS) are presented in Figure 3, as well as the relation between isotropic chemical shift and unit cell volumes. For all members of the A_2PtI_6 series only a single Pt site was observed, in agreement with the crystallographic studies. A clear monotonic upfield shift with increasing countercation size is evident, as well as significant differences in chemical shielding anisotropy (CSA) and linewidths. Lineshape and CSA

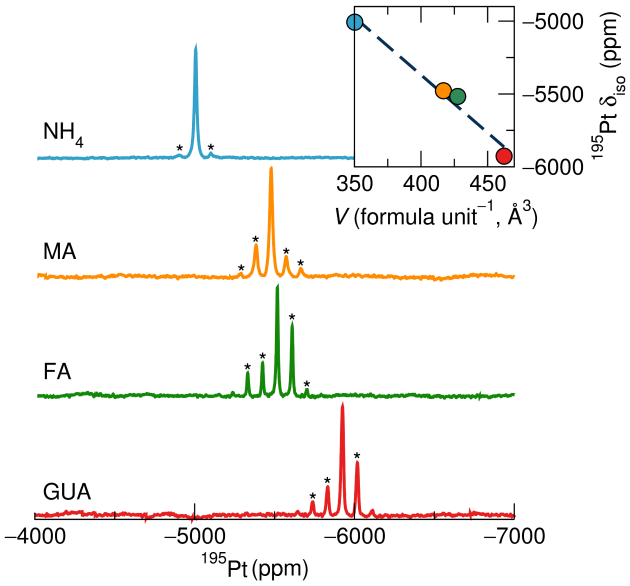

Figure 3: Room temperature 10 kHz MAS ^{195}Pt NMR spectra of A_2PtI_6 showing the influence of the countercation on chemical shift and lineshape. Asterisks indicate spinning sidebands, shifts are referenced to a 1 M solution of Na_2PtCl_6 in D_2O (0 ppm), and the field is 11.7 T (500 MHz for ^{1}H). Inset: Isotropic ^{195}Pt chemical shift, δ_{iso}, is correlated with unit cell volume per formula unit, V / F.U. A dashed line is drawn as a visual guide.

parameters are given in Table S4 in the Supporting Information and correlate well with Pt site symmetries from X-ray diffraction..

Table 1: ^{1}H longitudinal relaxation times, T_1, for A_2PtI_6 phases, with confidence intervals expressed as $\pm$ 1σ.

A	**^{1}H T_1 (s)**
NH_4	6.18 $\pm$ 0.07
MA	5.66 $\pm$ 0.24
FA	1.35 $\pm$ 0.01
GUA	0.598 $\pm$ 0.004

^{1}H inversion recovery experiments were conducted to assess the degree of molecular motion in the A_2PtI_6 phases (Figure S6), and resulting longitudinal relaxation times, T_1, are given in Table 1. We observe that T_1 is substantially longer in the ammonium and methylammonium phases. The theory of Bloembergen, Purcell, and Pound (BPP)[57] has been applied to establish molecular correlation times in similar compounds,[58–62] because in these plastic crystals, longitudinal relaxation is usually mediated by ^{1}H dipolar inter-

actions that fluctuate due to molecular motion. In the "fast motion" limit ($\omega_0\tau_C \ll 1$, where ω_0 is the nuclear Larmor frequency and τ_C is the autocorrelation time for molecular motion) which is valid for similar plastic crystals at ambient temperature, the expression for longitudinal relaxation time in BPP theory reduces $\tau_C \propto T_1^{-1}$. While there are small differences in the proportionality prefactor related to dipole-dipole separation, the substantially longer T_1 values for the ammonium and methylammonium phases imply more rapid molecular motion (short τ_C) compared to the FA and GUA compounds, which may be expected simply on the basis of molecular size. However, it is well known that strong hydrogen bonding of cations like FA and GUA can produce rigid structures, as seen in formate based perovskites,[63,64] or in the recently reported high-temperature ferroelectric material (3-ammoniopyrrolidinium)$RbBr_3$.[65] Furthermore, when compared to MA and FA lead iodide perovskites ($A$$PbI_3$) where the molecular cations are known to reorient at room temperature (and below),[62] these two compounds only undergo phase transitions to structures with cation disorder when brought to well above room temperature (Supporting Information).

To better understand if hydrogen bonding can explain the suspected reduced molecular motion of the cations in $(FA)_2PtI_6$ and $(GUA)_2PtI_6$, we examined how hydrogen bonds arrange in *ab initio* relaxed structures. Figure 4 shows crystallographic depictions of of $(FA)_2PtI_6$ and $(GUA)_2PtI_6$ (including hydrogen bonds). It can be seen in Figure 4(a) that FA cations hydrogen bond with iodides on $[PtI_6]^{2-}$ octahedra to form a connected network, and in Figure 4(b), how a representative $[PtI_6]^{2-}$ octahedron is surrounded by the FA cations. Each FA cation forms a total of 4 hydrogen bonds (N–H$\cdots$I), two to two iodides on one $[PtI_6]^{2-}$ octahedron (with bond lengths of 2.71 Å and 2.84 Å), and two "bridging bonds" to two other iodides on two separate neighboring $[PtI_6]^{2-}$ octahedra (bond lengths of 2.68 Å and 2.80 Å). These bridging bonds have been labeled in Figures 4(a) and (b) where visible, and are responsible for linking the discrete $[PtI_6]^{2-}$ octahedra together. All of these bonds create a 3D connected hydrogen bond network for $(FA)_2PtI_6$, suggesting that

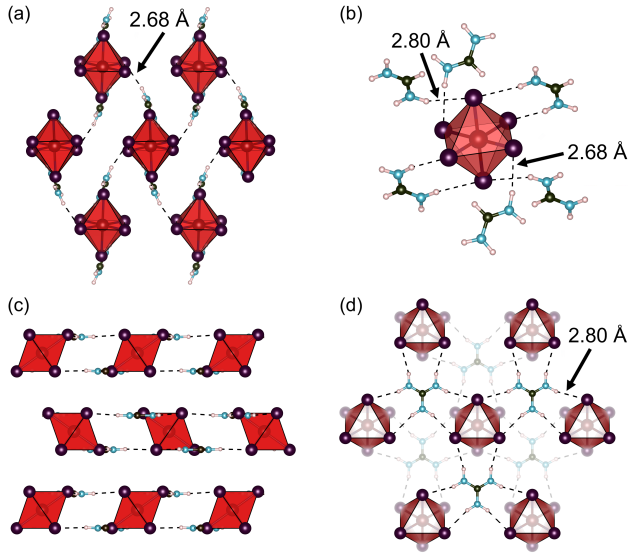

Figure 4: Crystallographic depictions of *ab initio* relaxed structures of $(FA)_2PtI_6$ [(a) and (b)] and $(GUA)_2PtI_6$ [(c) and (d)] illustrating their hydrogen bond networks. (a) View of the 3D connected network of hydrogen bonds linking $[PtI_6]^{2-}$ octahedra in $(FA)_2PtI_6$. The hydrogen bond length of all shown in (a) is 2.68 Å . (b) View of a representative $[PtI_6]^{2-}$ octahedron in $(FA)_2PtI_6$ with FA cations that hydrogen bond to it. (c) View of the 2D connected network of hydrogen bonds linking $[PtI_6]^{2-}$ octahedra in $(GUA)_2PtI_6$. (d) View along the layering direction of GUA cations hydrogen bonding to nearby $[PtI_6]^{2-}$. Each GUA cation bonds to a total of six iodides on three separate $[PtI_6]^{2-}$ octahedra.

hydrogen bonding may contribute substantially to the suspected reduced molecular motion of the formaminidinium cation. Figure 4(c) shows the 2D hydrogen bond network formed in $(GUA)_2PtI_6$, and Figure 4(d) illustrates a top-down view emphasizing the orientation of the GUA cations in relation to nearby $[PtI_6]^{2-}$ octahedra. Figure 4(c) displays a 2D connected network of hydrogen bonded GUA cations and $[PtI_6]^{2-}$ octahedra, where each GUA cation hydrogen bonds to a total of six iodides on three separate $[PtI_6]^{2-}$ octahedra. In Figure 4(d), one can see how there are two guanidiniums layers per one layer of $[PtI_6]^{2-}$ octahedra. Similar to the hydrogen bonding seen in $(FA)_2PtI_6$, we find that the location of the bonds in $(GUA)_2PtI_6$ help explain the suspected reduced molecular motion of the organic cation, as each hydrogen on the guanidinium cations aligns directly with a nearby $[PtI_6]^{2-}$ iodide. Indeed, we believe it is not a coincidence that the space group symmetry of $(GUA)_2PtI_6$ is compatible with the shape of the GUA cation. From this examination, we believe that the hydrogen bonds formed by these large organic cations actually dictate the observed structural trends in $(FA)_2PtI_6$ and $(GUA)_2PtI_6$.

Furthermore, the hypothesis of reduced motion in the FA and GUA compounds is consistent with the analysis of hydrogen bonding geometries. Steiner has reported average hydrogen bond donor$\cdots$acceptor and H$\cdots$acceptor distances based on a crystallographic database analysis of crystal structures determined by neutron diffraction.[66] The donor$\cdots$acceptor distances reported here are very similar for $-\mathrm{N}sp^2\mathrm{H}_2$ and $-\mathrm{N}^+\mathrm{H}_3$ donors and iodide acceptors ($\approx$3.7 Å). Donor$\cdots$acceptor distances in the X-ray crystal structures of the A_2PtI_6 phases presented are similar for FA and GUA (3.63 Å and 3.76 Å respectively), while those for ammonium (3.95 Å) fall outside the reported distribution, and the donor–H$\cdots$acceptor bond angles for methylammonium (139°) are outside the range considered by Steiner. This analysis would suggest that molecular motion could be uninhibited in the ammonium phase, while hydrogen bonding to the neighboring anions significantly restricts molecular motion in the FA and GUA phases.

The electronic band structures of the A_2PtI_6 phases, calculated within the framework

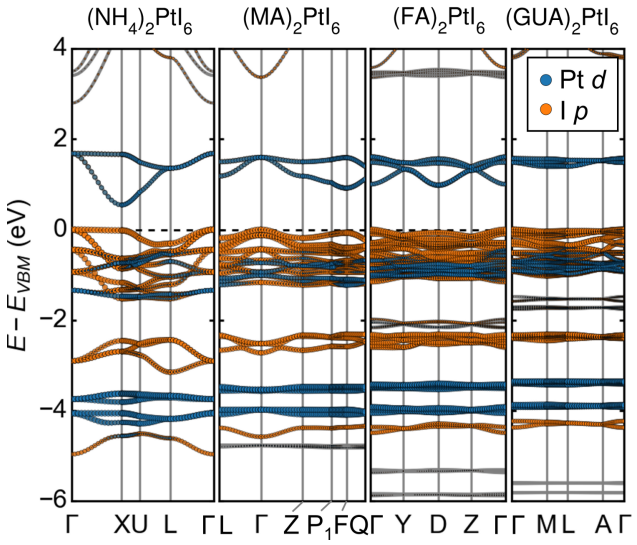

Figure 5: Electronic band structures (GGA-PBE) for A_2PtI_6 phases, illustrating decreasing bandwidths (and increasing bandgaps) with increasing countercation size. Orbital projections of Pt d character and I p character are presented as colored markers of variable size. In all cases, the valence bands derive primarily from the 5p orbitals of I, while the conduction bands derive from the unoccupied Pt 5d orbitals with irrep e_g. The effect of spin-orbit coupling is shown to be modest (see Figure S9). Energies are referenced to the valence band maximum for each phase.

of density functional theory (DFT), are presented in Figure 5 (details are provided in the Supporting Information). In all cases, the bandgap is between filled I p orbitals and empty Pt e_g orbitals, as expected for a low spin d^6 $[PtI_6]^{2-}$ polyanion. The valence and conduction bands across the series of compounds display diminished dispersion as one traverses across from the smaller $A = NH_4^+$ cation to MA and FA. In the hexagonal structure of $(GUA)_2PtI_6$, the valence and conduction bands are nearly fully localized. For the smaller *A* cations, the iodine sublattice is essentially close-packed, leading to overlap of the large 5p orbitals between neighboring $[PtI_6]^{2-}$ anions. For the undistorted $(NH_4)_2PtI_6$, despite the extended interactions being non-bonded the conduction bandwidth ($\approx$1 eV) is significant, and despite the central cation being different, it is similar to those reported for isostructural Cs_2SnI_6 and Cs_2TeI_6 where delocalized states similarly emerge due to iodine close-packing.[28–30] In all cases the bandgaps are indirect, but there are direct transitions that are only slightly higher in energy, as discussed in the Supporting Information. Ad-

ditionally, the electronic bandgaps and line-effective masses for electrons and holes are given in Tables S5 and S6 in the Supporting Information, together with cell volumes from *ab initio* structure relaxation. The computed band structures also offer an explanation for the downfield ^{195}Pt chemical shift with decreasing countercation size. The increasingly delocalized electronic states from closer intermolecular contact draw some charge density away from the Pt nucleus and into the intermolecular regions, deshielding the Pt nucleus.

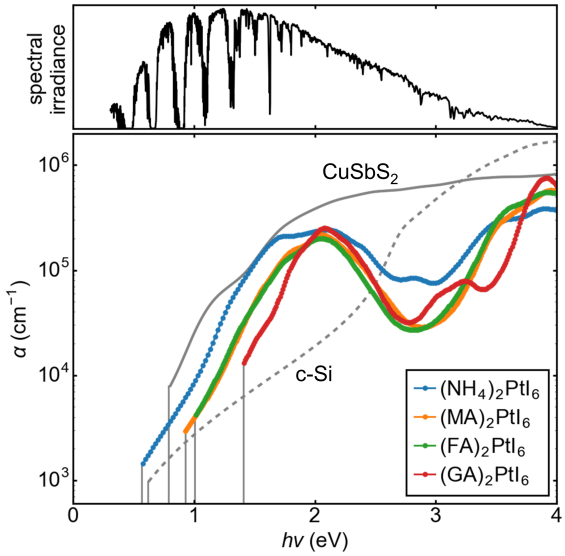

Figure 6: Ab initio optical absorption coefficients (GGA-PBE) for A_2PtI_6 phases, with bandgaps indicated by vertical gray lines. Indirect gap crystalline silicon (c-Si, dashed gray line) and the strongly absorbing direct gap chalcogenide $CuSbS_2$ (solid gray line) are included for comparison. Absorption in the violet/near-UV is poor for the A_2PtI_6 phases due to the paucity of available states immediately above the unoccupied Pt e_g states.

Optical absorption coefficients for the A_2PtI_6 series are displayed in Figure 6. Values for weakly absorbing c-Si and strongly absorbing $CuSbS_2$,[67] calculated similarly, are given for comparison. Additionally, the spectral dependence for solar irradiance (direct+diffuse at global tilt, ASTM G173-03) is included for reference.[68] For all of the Pt(IV) iodides, the absorption onset is rather strong despite their indirect bandgaps, reflecting a relatively high joint density of states near the band gap due to the partially localized nature of the electronic structure. The $A = NH_4^+$ compound, with the most disperse bands, displays

the lowest-energy absorption edge, as expected from the band structure. The A = MA and FA compounds display very similar calculated absorption edges and the A = GUA compound has the highest-energy absorption edge, in keeping with its more molecular nature. Despite slight differences in the near-IR and red due to the modestly differing bandwidths, the A_2PtI_6 phases exhibit very similar absorption around 2 eV, reflecting the similar underlying molecular character. Absorption is weak for these phases in the violet and near-UV, a consequence of the wide gap between the Pt e_g conduction bands and the next higher lying excited states.

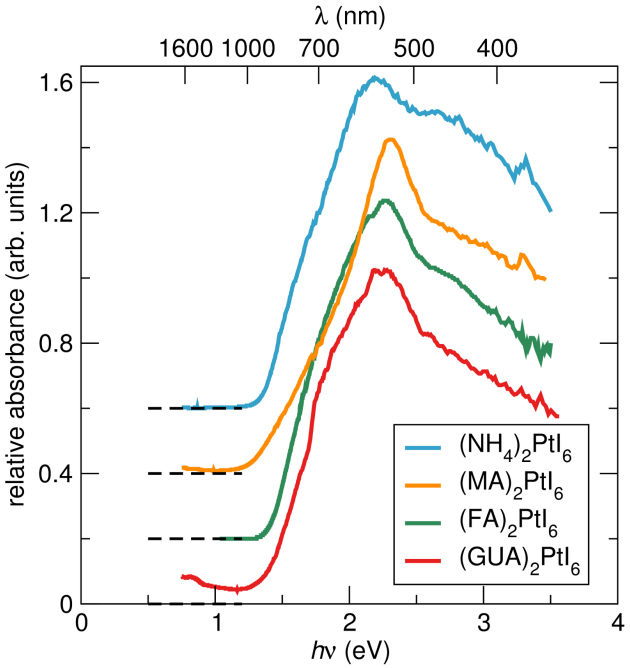

Figure 7: Normalized optical absorption spectra of the title compounds recorded on powders, obtained from Kubelka-Munk transformation of UV-vis diffuse reflectance powder spectra.

Experimental optical absorption spectra are displayed in Figure 7. The observed absorption onsets across the different compounds appear to be quite similar, exhibiting a peak in the absorption about 1 eV above the absorption edge, similar to what was calculated for these compounds. The red-shift of the peak in the calculated spectra when compared with experiment is consistent with the functionals employed here in the DFT calculation. The more disperse valence and conduction bands calculated for the $A = NH_4^+$ compound

give rise to the slightly sharper absorption edge, at lower energy than seen for the other compounds.

Conclusion

A study of the evolution of structure and properties the compounds A_2PtI_6 series, where *A* NH_4^+, MA, FA, and GUA suggests the importance of hydrogen-bonding for stabilizing some of the structure with the larger *A*-cations and the role of non-bonded I^-–I^- interactions in establishing relatively disperse electronic bands for the compounds with the smaller *A*-cations. We describe how as cation size increases, the structures undergo progressive distortion from the parent cubic vacancy-ordered double perovskite K_2PtCl_6-type structure, until converting to the the K_2MnF_6 structure type with $(GUA)_2PtI_6$. Analysis of ^{1}H ssNMR T_1 relaxation times and *ab initio* relaxed structures of $(FA)_2PtI_6$ and $(GUA)_2PtI_6$ suggest that FA and GUA cations engage in strong hydrogen bonding interactions with nearby iodide atoms on separate $[PtI_6]^{2-}$ octahedra, causing reduced cation molecular motion and distinct structural signatures at room temperature. The hydrogen bonds appear to guide the final structure formation for the FA and GUA compounds, with structures that can be best described as hydrogen-bonded networks. From DFT calculations, it is found that the intermolecular contact through close-packed iodide anions leads to dispersive frontier bands for the phases with smaller molecular ions.

Associated Content

Supporting Information

Supporting Information is available free of charge on the ACS Publications website at DOI:, containing details of the crystallography, powder X-ray diffraction attesting to the

purity of powders, details of the NMR studies, further details on the electronic structure, thermogravimetric analysis, and differential scanning calorimetry data.

Acknowledgments

This work was supported by the U.S. Department of Energy, Office of Science, Basic Energy Sciences under award number DE-SC-0012541. Extensive use of the Shared Experimental Facilities of the Materials Research Science and Engineering Center (MRSEC) at UCSB (NSF DMR 1720256) is gratefully acknowledged. The UCSB MRSEC is a member of the NSF-supported Materials Research Facilities Network (www.mrfn.org). We additionally acknowledge support from the Center for Scientific Computing at UCSB, supported by the NSF CNS-1725797 and NSF DMR-1720256. DHF thanks the National Science Foundation Graduate Research Fellowship Program for support under Grant DGE 1144085, and Raphaële Clément for helpful discussions. AKC thanks the Ras al Khaimah Centre for Advanced Materials for financial support.

References

(1) Kojima, A.; Teshima, K.; Shirai, Y.; Miyasaka, T. Organometal Halide Perovskites as Visible-Light Sensitizers for Photovoltaic Cells. *J. Am. Chem. Soc.* **2009**, *131*, 6050–6051.

(2) Lee, M. M.; Teuscher, J.; Miyasaka, T.; Murakami, T. N.; Snaith, H. J. Efficient Hybrid Solar Cells Based on Meso-Superstructured Organometal Halide Perovskites. *Science* **2012**, *338*, 643–647.

(3) Saliba, M.; Matsui, T.; Seo, J.-Y.; Domanski, K.; Correa-Baena, J.-P.; Nazeeruddin, M. K.; Zakeeruddin, S. M.; Tress, W.; Abate, A.; Hagfeldt, A.; Grätzel. Cesium-

Containing Triple Cation Perovskite Solar Cells: Improved Stability, Reproducibility and High Efficiency. *Energy Environ. Sci.* **2016**, *9*, 1989–1997.

(4) Fabini, D. H.; Labram, J. G.; Lehner, A. J.; Bechtel, J. S.; Evans, H. A.; Van der Ven, A.; Wudl, F.; Chabinyc, M. L.; Seshadri, R. Main-Group Halide Semiconductors Derived from Perovskite: Distinguishing Chemical, Structural, and Electronic Aspects. *Inorg. Chem.* **2017**, *56*, 11–25.

(5) Yang, W. S.; Park, B-W.; Jung, E. H.; Jeon, N. J.; Kim, Y. C.; Lee, D. U.; Shin, S. S.; Seo, J.; Kim, E. K.; Noh, J. H.; Seok, S. I. Iodide Management in Formamidinium-Lead-Halide Based Perovskite Layers for Efficient Solar Cells. *Science* **2017**, *356*, 1376–1379.

(6) Li, W.; Wang, Z.; Deschler, F.; Gao, S.; Friend, R. H.; Cheetham, A. K. Chemically Diverse and Multifunctional Hybrid Organic-Inorganic Perovskites. *Nat. Rev. Mater.*, **2**, 16099.

(7) Saparov, B.; Mitzi, D. B. Organic-Inorganic Perovskites: Structural Versatility for Functional Materials Design. *Chem. Rev.* **2016**, *116*, 4558–4596.

(8) Kubicki, D. J.; Prochowicz, D.; Hofstetter, A.; Saski, M.; Yadav, P.; Bi, D.; Pellet, N.; Lewiński, J.; Zakeeruddin, S. M.; Grätzel, M.; Emsley, L. Formation of Stable Mixed Guanidinium?Methylammonium Phases with Exceptionally Long Carrier Lifetimes for High-Efficiency Lead Iodide-Based Perovskite Photovoltaics. *J. Am. Chem. Soc.* **2018**, *140*, 3345–3351.

(9) Soe, C. M. M.; Stoumpos, C. C.; Kepenekian, M.; Traoré, B.; Tsai, H.; Nie, W.; Wang, B.; Katan, C.; Seshadri, R.; Mohite, A. D.; Even, J.; Marks, T. J.; Kanatzidis, M. G. New Type of 2D Perovskites with Alternating Cations in the Interlayer Space, $(C(NH_2)_3)(CH_3NH_3)_nPb_nI_{3n+1}$: Structure, Properties, and Photovoltaic Performance. *J. Am. Chem. Soc.* **2017**, *139*, 16297–16309.

(10) Lehner, A. J.; Fabini, D. H.; Evans, H. A.; Hébert, C.-A.; Smock, S. R.; Hu, J.; Wang, H.; Zwanziger, J. W.; Chabinyc, M. L.; Seshadri, R. Crystal and Electronic Structures of Complex Bismuth Iodides $A_3Bi_2I_9$ (A = K, Rb, Cs) Related to Perovskite: Aiding the Rational Design of Photovoltaics. *Chem. Mater.* **2015**, *27* , 7137–7148.

(11) Wei, F.; Deng, Z.; Sun, S.; Zhang, F.; Evans, D. M.; Kieslich, G.; Tominaka, S.; Carpenter, M. A.; Zhang, J.; Bristowe, P. D.; Cheetham, A. K. Synthesis and Properties of a Lead-Free Hybrid Double Perovskite: $(CH_3NH_3)_2AgBiBr_6$. *Chem. Mater.* **2017**, *29*, 1089–1094.

(12) McClure, E. T.; Ball, M. R.; Windl, W.; Woodward, P. M. Cs_2AgBiX_6 (X = Br, Cl): New Visible Light Absorbing, Lead-Free Halide Perovskite Semiconductors. *Chem. Mater.* **2016**, *28*, 1348–1354.

(13) Slavney, A. H.; Hu, T.; Lindenberg, A. M.; Karunadasa, H. I. A Bismuth-Halide Double Perovskite with Long Carrier Recombination Lifetime for Photovoltaic Applications. *J. Am. Chem. Soc.* **2016**, *138*, 2138–2141.

(14) Duyker, S. G.; Hill, J. A.; Howard, C. J.; Goodwin, A. L. Guest-Activated Forbidden Tilts in a Molecular Perovskite Analogue. *J. Am. Chem. Soc.* **2016**, *138*, 11121–11123.

(15) Zhao, X-G.: Yang, D.; Sun, Y.; Li, T.; Zhang, L.; Yu, L.; Zunger, A. Cu-In Halide Perovskite Solar Absorbers. *J. Am. Chem. Soc.* **2017**, *139*, 6718–6725.

(16) Dickinson, R. G. The Crystal Structures of Potassium and Ammonium Chlorostannates. *J. Am. Chem. Soc.* **1922**, *44*, 276–288.

(17) Armstrong, R. L. Structural Properties and Lattice Dynamics of 5d Transition Metal Antifluorite Crystals. *Phys. Rep.* **1980**, *57*, 343–396.

(18) Krupski, M. Rigid Sphere Model Applied to the Phase Transitions of Complex Compounds of the Type K_2PtCl_6. *Phys. Stat. Sol.* **1983**, *78*, 751–758.

(19) Prassides, K.; Day, P.; Cheetham, A. K. Anion Ordering in Mixed-Valence Cs_2SbCl_6 and Related Salts. *J. Am. Chem. Soc.* **1983**, *105*, 3366–3368.

(20) Kume, Y.; Ikeda, R.; Nakamura, D. Structural Phase Transition in Various Methylammonium Hexahalometallates(IV) as Studied by the NQR of Halogens. *J. Magn. Reson.* **1979**, *33*, 331–344.

(21) Ikeda, R.; Kume, Y.; Nakamura, D. Motion of Methylammonium Ions in Methylammonium Hexachloroplatinate(IV) and Hexachlorostannate(IV) as Studied by Proton Magnetic Resonance. *J. Magn. Reson.* **1976**, *24*, 9–20.

(22) Matsuo, T.; Yan, H-K.; Suga, H. Calorimetric Study of the Phase Transition in Deuterated Methylammonium Hexachlorostannate. *J. Phys. Chem. Solids* **1988**, *49*, 85–90.

(23) Matsuo, T.; Ueda, M.; Suga, H. Calorimetric and Spectroscopic Studies of the Critical Phase Transition in $(CH_3NH_3)_2[SnCl_6]$. *Chem. Phys. Lett.* **1981**, *82*, 577–580.

(24) Nakamura, D. Nuclear Quadrupole Resonance Studies of Structural and Magnetic Phase Transitions. *J. Mol. Struct.* **1975**, *111*, 341–356.

(25) Horiuchi, K.; Ishida, K.; Nakamura, D. A Temperature Dependence Study of ^{35}Cl NQR Frequencies in Dimethylammonium Hexachlorostannate(IV), Hexachlorotellurate(IV), and Hexachloroplatinate(IV). *Bull. Chem. Soc. Jpn.* **1985**, *58*, 2590–2594.

(26) Dillon, K. B.; Halfpenny, J.; Marshall, A. A Variable-Temperature ^{79}Br Nuclear Quadrupole Resonance and X-ray Crystallographic Investigation of Dimethylammonium Hexabromostannate(IV), $[NH_2Me_2]_2[SnBr_6]$. *J. Chem. Soc. Dalton Trans.* **1983**, *6*, 1091–1094.

(27) Murthy, B. V. S.; Ramesh, K. P.; Ramakrishna, J. NMR Study of Molecular Dynamics and Phase Transitions in Dimethyl Ammonium Hexabromo Selenate $[NH_2(CH_3)_2]_2SeBr_6$. *J. Phys. Chem. Solids* **2000**, *6*, 961–968.

(28) Lee, B.; Stoumpos, C. C.; Zhou, N.; Hao, F.; Malliakas, C.; Yeh, C.-Y.; Marks, T. J.; Kanatzidis, M. G.; Chang, R. P. H. Air-Stable Molecular Semiconducting Iodosalts for Solar Cell Applications: Cs_2SnI_6 as a Hole Conductor. *J. Am. Chem. Soc.* **2014**, *136*, 15379–15385.

(29) Maughan, A. E.; Ganose, A. M.; Bordelon, M. M.; Miller, E. M.; Scanlon, D. O.; Neilson, J. R. Defect Tolerance to Intolerance in the Vacancy-Ordered Double Perovskite Semiconductors Cs_2SnI_6 and Cs_2TeI_6. *J. Am. Chem. Soc.* **2017**, *138*, 8453–8464.

(30) Saparov, B.; Sun, J-P.; Meng, W.; Xiao, Z.; Duan, H-S.; Gunawan, O.; Shin, D.; Hill, I. G.; Yan, Y.; Mitzi, D. B. Thin-Film Deposition and Characterization of a Sn-Deficient Perovskite Derivative Cs_2SnI_6. *Chem. Mater.* **2016**, *28*, 2315–2322.

(31) Maughan, A. E.; Ganose, A. M.; Candia, A. M.; Granter, J. T.; Scanlon, D. O.; Neilson, J. R. Anharmonicity and Octahedral Tilting in Hybrid Vacancy-Ordered Double Perovskites. *Chem. Mater.* **2017** *30*, 472–483.

(32) Datta, R. L. The Double Platinic and Cupric Iodides of Substituted Ammonium Bases. *J. Chem. Soc., Trans.* **1913**, *103*, 426–432.

(33) Sutton, M.; Armstrong, R. L.; Powell, B. M.; Buyers, W. J. L. Neutron Diffraction tsudy of the Structural Changes in the Antifluorite Crystals Rb_2PtI_6, $(NH_4)_2PtBr_6$, and $(NH_4)_2PtI_6$. *Can. J. Phys.* **1981**, *59*, 449–456.

(34) Thiele, G.; Mrozek, C.; Kammerer, D.; Wittmann, K. On Hexaiodoplatinates (IV) M_2PtI_6 (M= K, Rb, Cs, NH_4, Tl)-Preparation, Properties and Structural Data. *Z. Naturforsch.* **1983**, *88b*, 905–910.

(35) SADABS; Sheldrich, G. M. University of Gottingen: Germany, **2005**.

(36) SHELXTL PC, Version 6.12; Bruker AXS Inc.: Madison, WI, **2005**.

(37) K. Momma, F. Izumi. An Integrated Three-Dimensional Visualization System VESTA Using WxWidgets. *Commission on Crystallogr. Comput.* **2006**, *7*, 106–119.

(38) Coelho, A. TOPAS and TOPAS-Academic: an Optimization Program Integrating Computer Algebra and Crystallographic Objects Written in C++. *J. Appl. Cryst.* **2018**, *51*, 210–218.

(39) Kresse, G.; Hafner, J. *Ab initio* Molecular Dynamics for Liquid Metals. *Phys. Rev. B* **1993**, *47*, 558–561.

(40) Kresse, G.; Hafner, J. *Ab initio* Molecular-Dynamics Simulation of the Liquid-Metal-Amorphous-Semiconductor Transition in Germanium. *Phys. Rev. B* **1994** *49*, 14251–14269.

(41) Kresse, G.; Furthmüller, J. Efficient Iterative Schemes for *Ab Initio* Total-Energy Calculations Using a Plane-Wave Basis Set. *Phys. Rev. B* **1996** *54*, 11169–11186.

(42) Kresse, G.; Furthmüller, J. Efficiency of ab-initio total energy calculations for metals and semiconductors using a plane-wave basis set. *Comput. Mater. Sci.* **1996**, *6*, 15–50.

(43) Blöchl, P. E. Projector Augmented-Wave Method. *Phys. Rev. B* **1996**, *50*, 17953–17979.

(44) Kresse, G.: Joubert, D. From Ultrasoft Pseudopotentials to the Projector Augmented-Wave Method. *Phys. Rev. B* **1999** *59*, 1758–1775.

(45) Perdew, J. P.; Burke, K.; Ernzerhof, M. Generalized Gradient Approximation Made Simple. *Phys. Rev. Lett.* **1997**, *77*, 3865–3868.

(46) Monkhorst, H. J.; Pack, J. D. Special Points for Brillouin-Zone Integrations.*Phys. Rev. B* **1976**, *13*, 5188–5192.

(47) Grimme, S.; Antony, J.; Ehrlich, S.; Krieg, H. A Consistent and Accurate *Ab Initio* Parametrization of Density Functional Dispersion Correction (DFT-D) for the 94 Elements H-Pu. *J. Chem. Phys.* **2010**, *132*, 154104-1–154104-19.

(48) Stokes, H. T.; Hatch, D. M. FINDSYM: Program for Identifying the Space-Group Symmetry of a Crystal. *J. Appl. Cryst.* **2005**, *38*, 237–238.

(49) Setyawan, W.; Curtarolo, S. High-Throughput Electronic Band Structure Calculations: Challenges and Tools. *Comput. Mater. Sci.* **2010**, *49*, 299–312.

(50) Gajdoš, M.; Hummer, K.; Kresse, G.; Furthmaller, J.; Bechstedt, F. Linear Optical Properties in the Projector-Augmented Wave Methodology. *Phys. Rev. B* **2006**, *73*, 045112-1–045112-9.

(51) Bukovec, P.; Hoppe, R. Zur Kenntnis Von Hexagonalem $K_2[MnF_6]$. *J Fluor. Chem.* **1983**, *23*, 579–587.

(52) Shannon, R.D.; Prewitt, C.T. Effective Ionic Radii in Oxides and Fluorides. *Acta. Crystallogr.* **1969**, *B25*, 925–946.

(53) Shannon, R.D. Revised Effective Ionic Radii and Systematic Studies of Interatomic Distances in Halides and Chalcogenides. *Acta. Crystallogr.* **1976**, *A32*, 751–767.

(54) Kieslich, G.; Sun, S.; Cheetham, A. K. Solid-State Principles Applied to Organic?Inorganic Perovskites: New Tricks for an Old Dog. *Chem. Sci.* **2014**, 5, 4712–4715.

(55) Maughan, A. E.; Ganose, A. M.; Almaker, M. A.; Scanlon, D. O.; Neilson, J. R. Tolerance Factor and Cooperative Tilting Effects in Vacancy-Ordered Double Perovskite Halides. *Chem. Mater.* DOI: 10.1021/acs.chemmater.8b01549.

(56) Muller, O.; Roy, R. The Major Ternary Structural Families (Crystal Chemistry of Non-Metallic Materials), 1st ed.; Springer-Verlag: Berlin, 1974.

(57) Bloembergen, N.; Purcell, E. M.; Pound, R. V. Relaxation Effects in Nuclear Magnetic Resonance Absorption. *Phys. Rev.* **1948**, *73*, 679–712.

(58) Wasylishen, R.E.; Knop, O.; Macdonald, J.B. Cation Rotation in Methylammonium Lead Halides. *Solid State Commun.* **1985**, *56*, 581–582.

(59) Senthil, S.; Ramesh, K.P.; Ramakrishna, J. Proton NMR T_1 Studies in Methylammonium Trichloro Stannate(II) ($CH_3NH_3SnCl_3$). *Phase Transitions* **2010**, *75*, 597–605.

(60) Besara, T.; Jain, P.; Dalal, N. S.; Kuhns, P. L.; Reyes, A. P. Kroto, H. B.; Cheetham, A. K. Mechanism of the Order-Disorder Phase Transition, and Glassy Behavior in the Metal-Organic Framework $[(CH_3)_2NH_2]Zn(HCOO)_3$. *Proc. Natl. Acad. Sci. U.S.A* **2011**, *108*, 6828–6832.

(61) Abhyankar, N.; Kweon, J. J.; Orio, M.; Bertaina, S.; Lee, M.; Choi, E. S.; Fu, R.; Dalal, N. S. Understanding Ferroelectricity in the Pb-Free Perovskite-Like Metal-Organic Framework $[(CH_3)_2NH_2]Zn(HCOO)_3$: Dielectric, 2D NMR, and Theoretical Studies. *J. Phys. Chem. C* **2017**, *121*, 6314–6322.

(62) Fabini, D. H.; Siaw, T. A.; Stoumpos, C. C.; Laurita, G.; Olds, D.; Page, K.; Hu, J. G.; Kanatzidis, M. G.; Han, S.; Seshadri, R. Universal Dynamics of Molecular Reorientation in Hybrid Lead Iodide Perovskites. *J. Am. Chem. Soc.* **2017**, *139*, 16875–16884.

(63) Li, W.; Thirumurugan, A.; Barton, P. T.; Lin, Z.; Henke, S.; Yeung, H. H.-M.; Wharmby, M. T.; Bithell, E. G.; Howard, C. J.; Cheetham, A. K. Mechanical Tunability Via Hydrogen Bonding in Metal-Organic Frameworks with the Perovskite Architecture. *J. Am. Chem. Soc.* **2014**, *136*, 7801–7804.

(64) Svane, K. L.; Forse, A. C.; Grey, C. P.; Kieslich, G.; Cheetham, A. K.; Walsh, A.; Butler, K. T. How Strong is the Hydrogen Bond in Hybrid Perovskites? *J. Phys. Chem. Lett.* **2017**, *8*, 6154–6159.

(65) Pan, Q.; Liu, Z-B.; Tang, Y-Y.; Li, P.F.; Ma, R.-W.; Wei, R-Y.; Zhang, Y.; You, Y-M.; Ye, H-Y.; Xiong, R.G. A Three-Dimensional Molecular Perovskite Ferroelectric:(3-Ammoniopyrrolidinium) $RbBr_3$. *J. Am. Chem. Soc.* **2017**, *139*, 3954–3957.

(66) Steiner, T. Hydrogen-Bond Distances to Halide Ions in Organic and Organometallic Crystal Structures: Up-to-date Database Study. *Acta Cryst.* **1998**, *B54*, 456–463.

(67) Yu, L.; Kokeyesi, R. S.; Keszler, D. A.; Zunger, A. Inverse Design of High Absorption Thin-Film Photovoltaic Materials. *Adv. Energy Mater.* **2013**, *3*, 43–48.

(68) National Renewable Energy Laboratory, Reference Solar Spectral Irradiance: ASTM G-173. http://rredc.nrel.gov/solar/spectra/am1.5/astmg173/astmg173.html (accessed 12/4/2017)

For Table of Contents

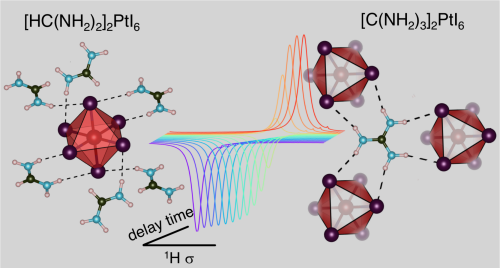

Solid state nuclear magnetic resonance and *ab initio* calculations help understand the role that hydrogen bonding interactions play in stabilizing the perovskite-derived structures of formamidinium and guanidinium platinum iodides.

Supporting Information for: Hydrogen Bonding Controls the Structural Evolution in Perovskite-Related Hybrid Platinum (IV) Iodides

Hayden A. Evans,[†,‡] Douglas H. Fabini,[¶,‡] Jessica L. Andrews,[†] Mitchell Koerner,[§] Molleigh B. Preefer,[†,‡] Guang Wu,[†] Fred Wudl,[¶] Anthony K. Cheetham,[‡,‖] and Ram Seshadri[*,†,¶,‡]

†*Department of Chemistry and Biochemistry*
University of California, Santa Barbara, California 93106, United States
‡*Materials Research Laboratory*
University of California, Santa Barbara, California 93106, United States
¶*Materials Department*
University of California, Santa Barbara, California 93106, United States
§*Physics Program, College of Creative Studies*
University of California, Santa Barbara, California 93106, United States
‖*Department of Materials Science and Engineering*
National University of Singapore, Singapore 117575.

E-mail: seshadri@mrl.ucsb.edu

Material descriptions

All structures reported were solved via single crystal X-ray diffraction with relevant crystallographic data summarized in Tables S1 and S2.

Table S1: Crystallographic Data for $(NH_4)_2PtI_6$ and $(MA)_2PtI_6$

Empirical Formula	$(NH_4)_2PtI_6$		$(CH_3NH_3)_2PtI_6$
Crystal habit, color	cubic, bronze		hexagonal, bronze
Crystal system	cubic	tetragonal	trigonal
Space group (#)	$Fm\bar{3}m$ (225)	$P4/mnc$ (128)	$R\bar{3}m$ (136)
Volume (Å^3)	1397(1)	681.6(1)	1250.5(2)
T (K)	290	100	273
a (Å)	11.179(4)	7.6446(5)	7.943(5)
b (Å)	11.179(4)	7.6446(5)	7.943(5)
c (Å)	11.179(4)	11.6625(9)	22.88(2)
α (°)	90	90	90
β (°)	90	90	90
γ (°)	90	90	120
Z	4	2	3
ρ (g mol^{-1})	984.51	985.52	1014.58
Dens. (g cm^{-3})	4.681	4.802	4.042
Abs. (mm^{-1})	23.257	23.834	19.491
F_{000}	1640	822	1284
Reflections (unique)	1167(175)	5177(532)	2643(423)
R_{int}	0.0523	0.0305	0.0443
R_1	0.0518	0.0291	0.0412
wR_R	0.0954	0.0513	0.1137
∂F (eÅ^{-3})	1.117 & −6.062	1.637 & −3.065	1.132 & −2.843
GOF	1.102	1.388	0.905

Figure S1(a) displays the 300 K structure of $(NH_4)_2PtI_6$ which crystallizes in the space group $Fm\bar{3}m$ and is isostructural to the VDHP K_2PtCl_6. In this structure, Pt and I are found on face-centered cubic lattices with ammonium cations in tetrahedral cavities.[1,2] Figure 1(b) presents the 100 K structure, space group $P4/mnc$. At low temperature $(NH_4)_2PtI_6$ distorts similar to other perovskites with an in phase octahedral rotation parallel to the c-axis, described by Glazer tilting nomenclature as a $a^0a^0c^+$ distortion.[3]

Figure S2 illustrates the 300 K structure of $(MA)_2PtI_6$, space group $R\bar{3}m$. We observe

Table S2: Crystallographic Data for $(FA)_2PtI_6$ and $(GUA)_2PtI_6$.

Empirical Formula	$[CH(NH_2)_2]_2PtI_6$		$[C(NH_2)_3]_2PtI_6$
Crystal habit, color	needle, bronze		block, bronze
Crystal system	monoclinic	tetragonal	hexagonal
Space group (#)	$P2_1/n$ (14)	$I4/m$ (87)	$P63mc$ (186)
Volume (Å^3)	855.0(2)	859(3)	924.8(3)
T (K)	100	350	100
a (Å)	7.679(2)	9.65(2)	9.369(2)
b (Å)	13.360(3)	9.65(2)	9.369(2)
c (Å)	8.572(2)	9.21(2)	12.164(2)
α (°)	90	90	90
β (°)	108.695(9)	90	90
γ (°)	90	90	120
Z	2	2	2
ρ (g mol^{-1})	1046.63	1041.59	1076.67
Dens. (g cm^{-3})	4.173	4.027	3.866
Abs. (mm^{-1})	19.516	18.923	17.588
F_{000}	892	882	924
Reflections (unique)	7379(2049)	956(459)	4907(1083)
R_{int}	0.0316	459	0.0335
R_1	0.0271	0.0736	0.0256
wR_R	0.0577	0.1798	0.0606
∂F ($e\mathring{A}^{-3}$)	1.313 & -2.026	1.775 & -1.275	1.992 & -1.654
GOF	1.235	1.104	1.047

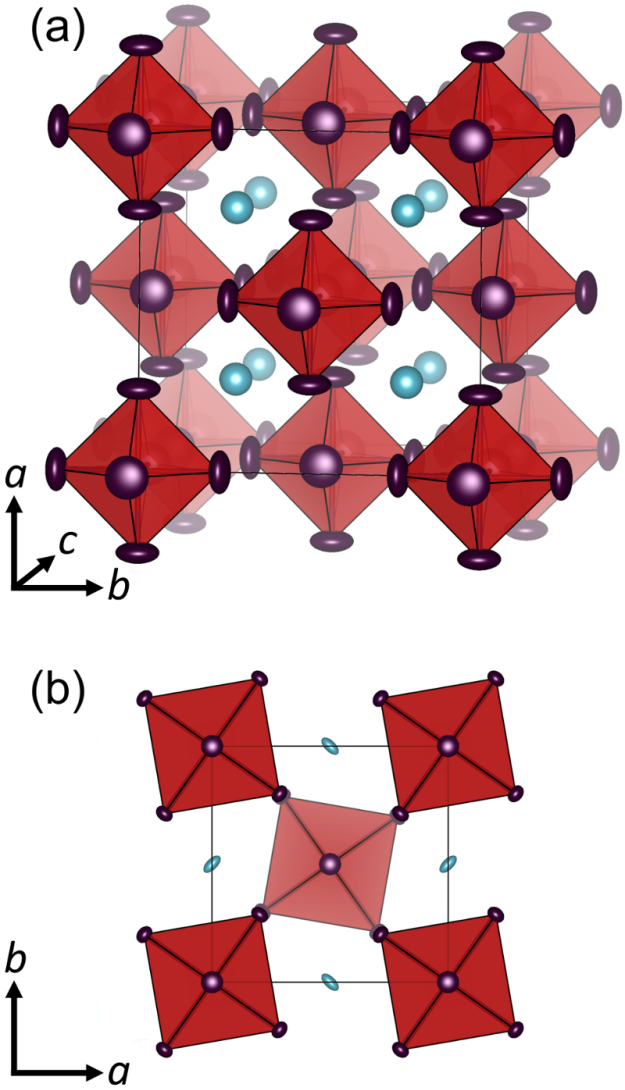

Figure S1: Crystal structure of $(NH_4)_2PtI_6$ with displacement ellipsoids (95% probability). (a) 300 K structure, viewed along c-axis, (b) 100 K structure, viewed along the c-axis to emphasize octahedral titling.

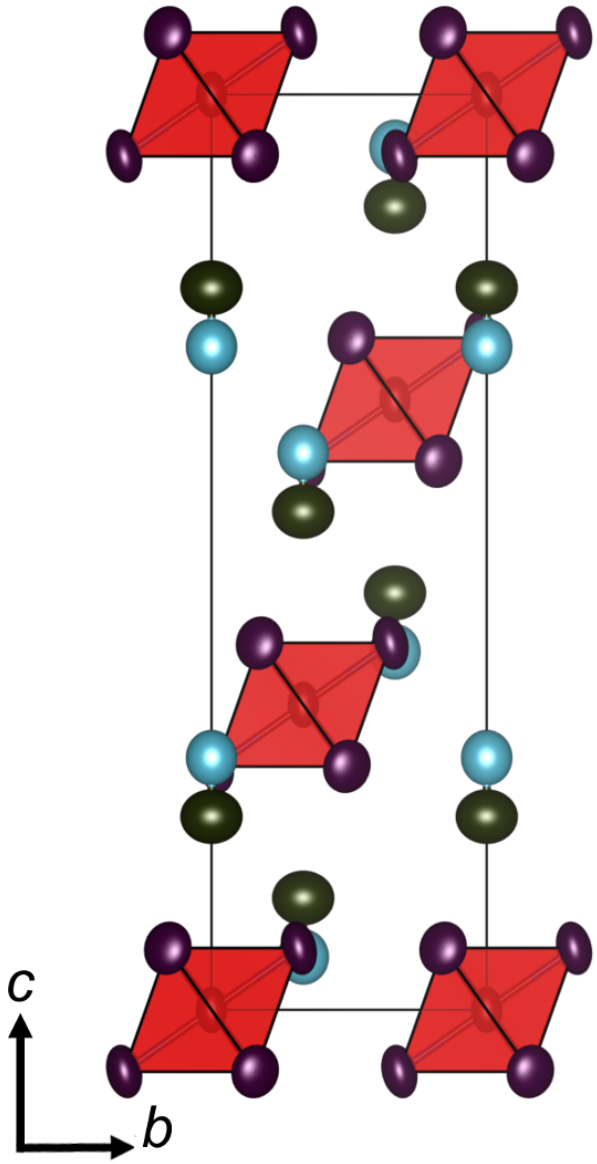

Figure S2: Crystal structure of $(MA)_2PtI_6$ at 300 K, with displacement ellipsoids (95% probability), viewed down along a-axis.

no first-order phase transition between 100 K and 480 K, though a second-order phase transition has previously been suggested at 134 K.[4,5] The platinum ions in $(MA)_2PtI_6$ are found on Wyckoff site $3a$ with site symmetry $\bar{3}m$, and iodide ions are found on Wyckoff site $18h$ with site symmetry $.m$. The methylammonium cations are modeled here as static molecules aligned parallel to the *c*-axis.

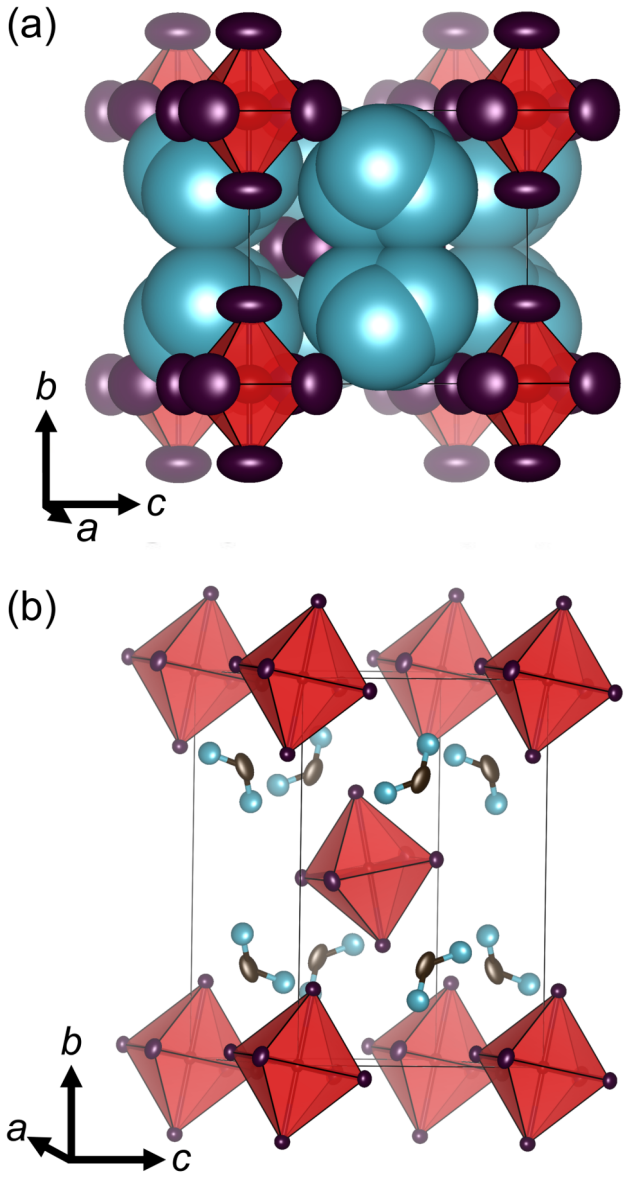

Figure S3: Crystal structure of $(FA)_2PtI_6$ with displacement ellipsoids (95% probability). (a) 340 K, viewed along a-axis. (b) 100 K and below, viewed down a-axis.

Figure S3 depicts the high temperature (340 K and warmer) and low temperature

(340 K to 100 K) structures of $(FA)_2PtI_6$. Some of the authors previously reported a compound of this empirical formula as isostructural to K_2PtI_6, but upon NMR analysis concluded this was incorrect. It was found that formamidinium ions degraded in solution (if the reaction temperature was brought above 70°C), yielding free NH_4^+ cations, which precipitate from solution in the form of $(NH_4)_2PtI_6$. If the solution is kept above 70°C for 20 minutes, $(NH_4)_2PtI_6$ is produced essentially pure. An erratum was submitted for the previous report.[8]

Figure S3(a) illustrates the high temperature phase of formamidinium platinum iodide, space group $I4/m$, viewed along the a-axis, depicting $[PtI_6]^{2-}$ octahedra and disordered formamidiniums. Platinum ions are found on Wyckoff site $2a$ with site symmetry $4/m..$, with two independent iodides residing on the $8h$ and $4e$ Wyckoff sites, site symmetry $m..$ and $4..$, respectively. Formamidinium cations are modeled as distorted tetrahedra. Figure S3(b) displays the low temperature structure of formamidinium platinum iodide, space group $P2_1/n$, illustrating canted octahedra and ordered formamidinium cations. The structure contains platinum ions on Wyckoff position $2a$ with site symmetry $\bar{1}$, and 3 independent iodide ions as well as formamidinium C and N atoms located on general positions $4e$. There are currently few reported formamidinium-containing VHDPs, but there are compounds that contain organic cations such as dimethylammonium which crystallize with similar structural motifs.[9,10]

Figure S4 displays the stable structure (between 100 K and 423 K) of $(GUA)_2PtI_6$, space group $P6_3mc$, viewed along the a-axis. Platinum ions are found on Wyckoff position $2b$ with site symmetry $3m.$ and iodide ions and carbon atoms are found on $6c$ positions, site symmetry $.m.$. There are two crystallographically distinct guanidinium cations within the unit cell of the compound, both of which are modeled here without disorder. The inorganic lattice is comprised of planes of similarly tilted $[PtI_6]^{2-}$ octahedra which alternate along the c-axis. $(GUA)_2PtI_6$ is similar to past reported guanidinium chloro- and bromometallate structures, though those reported consistently crystallize in the centrosymmetric space

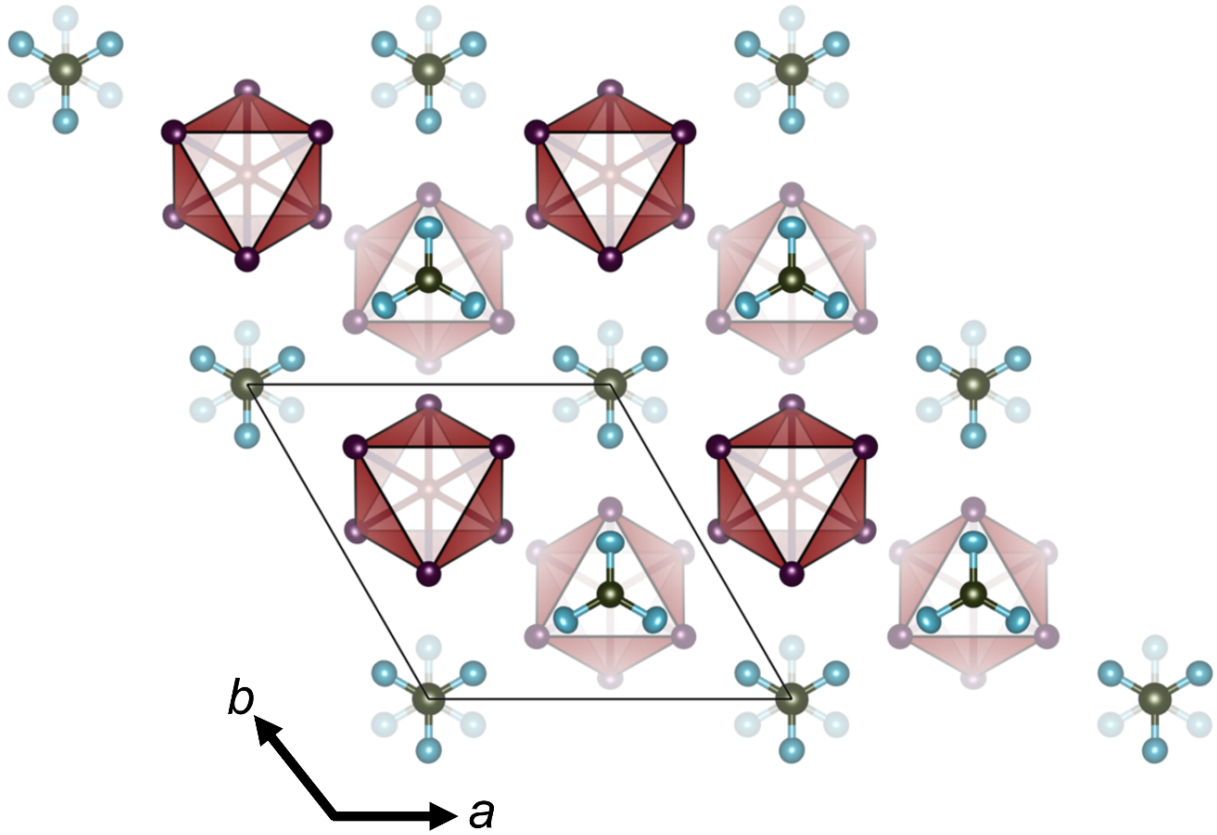

Figure S4: Crystal structure of $(GUA)_2PtI_6$ at 100 K, viewed along the c-axis, with displacement ellipsoids (95% probability).

group, $C2/m$.[11]

Powder X-ray Diffraction

Experimental laboratory PXRD data was Rietveld refined (without atomic occupancy) using room temperature single crystal diffraction as the structural comparison (Figure S5). The refinements indicate that the each bulk sample has unit cell parameters close to single crystal diffraction dimensions (Table S3 refined data, Tables S1 and S2 for single crystal data).

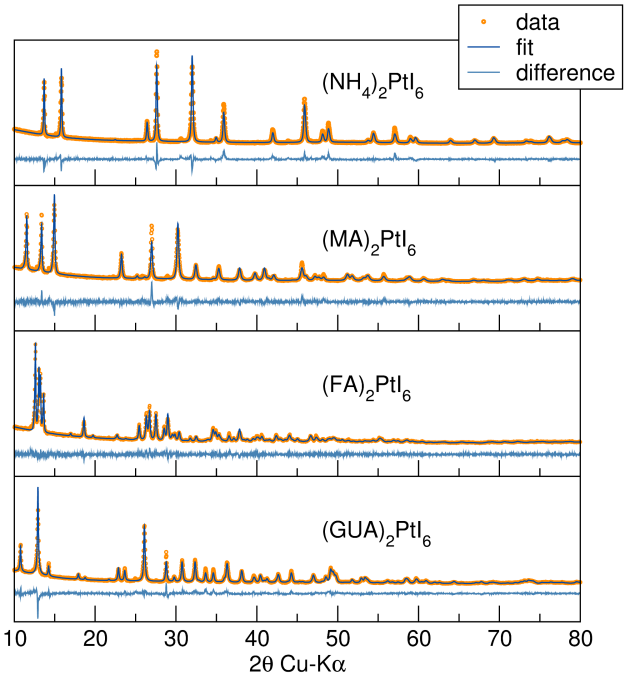

Figure S5: Rietveld refinements of the A_2PtI_6 compounds.

Table S3: Refined lattice parameters of A_2PtI_6 compounds.

Forumla	$(NH_4)_2PtI_6$	$(MA)_2PtI_6$	$(FA)_2PtI_6$	$(GUA)_2PtI_6$
a (Å)	11.175	7.955	7.790	9.424
b (Å)	11.175	7.955	13.512	12.377
c (Å)	11.175	22.918	8.630	9.424
α (°)	90	90	90	90
β (°)	90	90	109.1	90
γ (°)	90	120	90	120

Nuclear Magnetic Resonance (NMR)

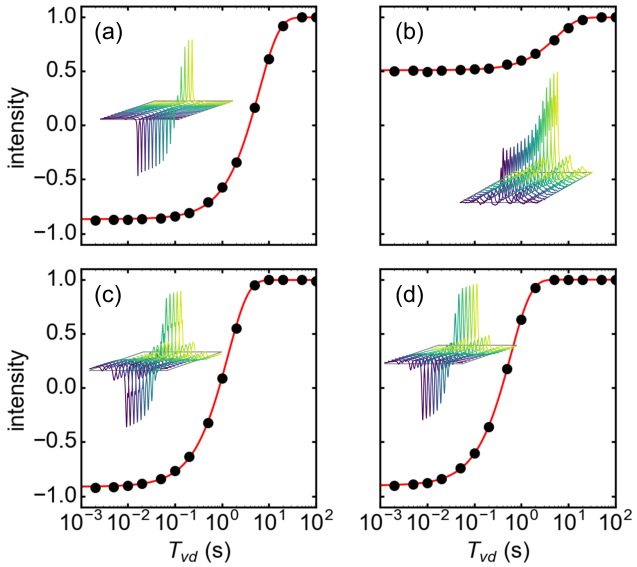

Figure S6: ^{1}H inversion recovery experiments of the A_2PtI_6 series. (a) $(NH_4)_2PtI_6$, (b) $(MA)_2PtI_6$, (c) $(FA)_2PtI_6$, (d) $(GUA)_2PtI_6$.

^{1}H inversion recovery experiments (Figure S6) were conducted to assess the degree of molecular motion in the A_2PtI_6 phases, and resulting longitudinal relaxation times, T_1, are given in Table 1 in the main text. We observe that T_1 is substantially longer in the ammonium and methylammonium phases, and reduced in the formamidinium and guanidinium phases.

^{1}H single-pulse NMR spectra under MAS for the A_2PtI_6 phases are presented in Figure S7. At these modest MAS speeds, ^{1}H dipolar interactions are only partially averaged out, and the three chemically distinct protons of the formamidinium ion cannot be re-

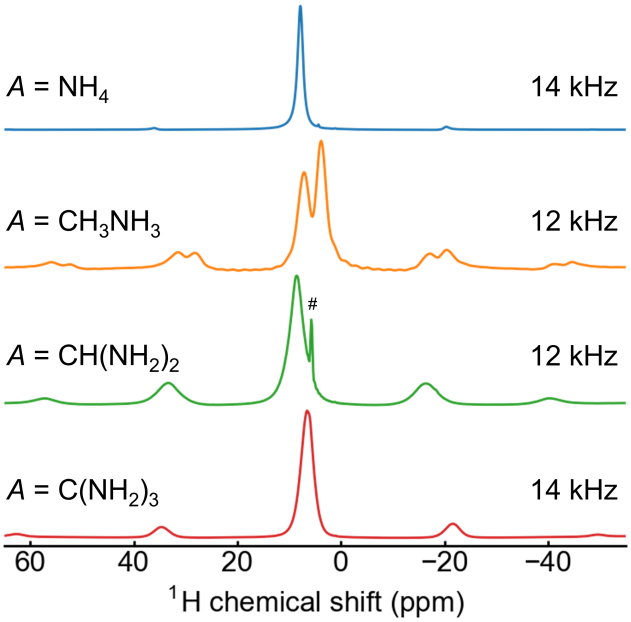

Figure S7: MAS ^{1}H NMR spectra of A_2PtI_6 phases, with spinning speed indicated. A small (3%), mobile impurity is evident in $(FA)_2PtI_6$ at 5.7 ppm, potentially from a NH_4 impurity generated through degradation of the formamidinium precursor. At this modest speed, strong ^{1}H dipolar interactions prevent resolution of the three chemically distinct protons on the formamidinium ion which are evident in solution. As $[NH_4]^+$ and $[GUA]^+$ each have one distinct proton, the broader signal for guanidinium suggests a reduced state of molecular motion.

solved.

Table S4: ^{195}Pt NMR lineshape parameters for A_2PtI_6 phases, Pt site symmetry from X-ray diffraction, and experimental and *ab initio* $[PtI_6]^{2-}$ octahedral volumes, V_{oct}. Ω = Guassian broadening. Ψ = Pt site symmetry

A	δ_{iso} **(ppm)**	δ_{CSA} **(ppm)**	η	Ω **(Hz)**	Ψ	**Expt.** V_{oct} **(Å)**	**Calc.** V_{oct} **(Å)**
NH_4	−5006	59	0.001	1963	$m\bar{3}m$	25.32	26.34
MA	−5478	166	0.106	2377	$\bar{3}m$	25.43	26.49
FA	−5518	218	−0.009	1066	$\bar{1}$	25.80	26.60
GA	−5926	196	0.224	1397	$3m.$	25.42	26.51

^{195}Pt lineshape and CSA parameters are given in Table S4, together with the Pt site symmetry from X-ray diffraction and the experimental and *ab initio* (vide infra) $[PtI_6]^{2-}$ octahedral volumes. The CSA parameters correlate well with Pt site symmetry, with the smallest δ_{CSA} for the highest site symmetry ($m\bar{3}m$), and the largest δ_{CSA} for the lowest Pt site symmetry ($\bar{1}$). While no CSA would be expected for Pt in the ammonium phase, due to the octahedral site symmetry, very small sidebands are observed. These likely arise from residual heteronuclear dipolar coupling, spin-orbit coupling, or other sources of broadening. The Gaussian broadening parameters extracted in lineshape fitting indicate broader lines in the ammonium and methylammonium phase. The origin of this behavior is not immediately apparent, as subsequent analysis of motion (*vide infra*) suggests that if anything, molecular motion is faster in these phases. In sum, no features are seen in NMR which suggest that the local environments of Pt deviate significantly from those in the crystallographic models.

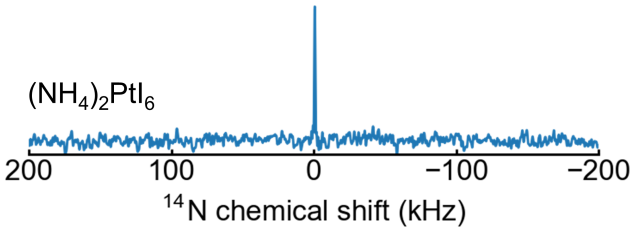

Figure S8: Spin-echo ^{14}N (S = 1) experiment for $(NH_4)_2PtI_6$, showing a narrow signal due to the tetrahedral molecular symmetry of the NH_4^+ cation.

Spin-echo ^{14}N (S = 1) experiments were additionally carried out (Figure S8) on the

A_2PtI_6 phases, leveraging the quadrupole moment as a probe of motion. A narrow signal was easily observed for $A = NH_4$ due to the tetrahedral molecular symmetry, while no signals were detected for the other three phases within one hour of acquisition. This result would be consistent with insufficiently rapid molecular motion to average out strong quadrupolar interactions, which are not already canceled due to the lower symmetry N environments in these molecules, though we cannot postulate more quantitative results without protracted experiments to acquire these (presumably) extremely broad signals.

Electronic Structure

The electronic band structures of the A_2PtI_6 phases, calculated within the framework of density functional theory (DFT), are presented in Figure 4 in the main text. Crystal structures were relaxed including semi-empirical van der Waals corrections, and the exchange-correlation energy was treated with the generalized gradient approximation (GGA; full computational details in the Methods section above).

The electronic bandgaps and line effective masses for electrons and holes (not the density of states effective masses) are given in Table S5, together with cell volumes from *ab initio* structure relaxation in Table S6. For the A_2PtI_6 phases, bandgaps and effective masses increase monotonically with countercation size, consistent with our discussion of intermolecular I–I contact. Bandgaps are indirect in all cases, with the valence band maxima occurring at the zone centers. No pattern in the locations of the conduction band minima is readily apparent without detailed analysis of the spatial relationship between the Brillouin zones of the different lattice types. Despite the use of van der Waals corrections, the DFT relaxed structures overestimate unit cell volumes by 9% to 17% (corresponding to 3% to 5% linear), in line with the known underbinding of the GGA.

For $(NH_4)_2PtI_6$, the valence band is $\sim$19 meV higher at Γ than at X, while the conduction band minimum occurs at X. This phase then has an indirect bandgap, but the direct

Table S5: Calculated electronic bandgaps (E_g) and line effective masses (m_e^*, m_h^*) for members of the A_2PtI_6 series. For line effective masses, the first Brillouin zone special point labels the band extremum, and the second special point indicates the direction from the extremum along which the dispersion is fitted.

Phase	E_g (eV)	VBM	CBM	m_e^* / m_0	m_h^* / m_0
$(NH_4)_2PtI_6$	0.55	Γ	X	X→Γ: 0.43	Γ→X (light): 0.64
				X→W: 0.39	Γ→X (heavy): 25.3
				X→U: 0.38	Γ→K (light): 0.64
					Γ→K (medium): 0.92
					Γ→K (heavy): 1.90
					Γ→L (light): 0.79
					Γ→K (heavy): 1.47
$(MA)_2PtI_6$	0.94	Γ	F	F→Q: 0.61	Γ→L: 1.29
				F→P_1: 0.74	Γ→Z: 1.29
					Γ→X: 2.30
$(FA)_2PtI_6$	1.00	Γ	D	D→Z: 0.78	Γ→Y: 1.75
				D→M: 0.87	Γ→X: 3.98
				D→Y: 0.61	Γ→Z: 1.74
$(GUA)_2PtI_6$	1.41	Γ	M	M→Γ: 3.46	Γ→M (light): 3.18
				M→K: 11.6	Γ→M (heavy): 6.08
				M→L: 32.2	Γ→K (light): 3.26
				K→M: 8.72	Γ→K (heavy): 5.97
				K→Γ: 3.41	Γ→A: 4.24
				K→H: 2.86	
				L→A: 2.05	
				L→H: 2.62	

Table S6: Calculated and experimental volume per formula unit (V / F.U.) for members of the A_2PtI_6 series.

Phase	**V / F.U. (Å^3), calc.**	**V / F.U. (Å^3), expt.**
$(NH_4)_2PtI_6$	382.2	350.25
$(MA)_2PtI_6$	475.1	416.83
$(FA)_2PtI_6$	501.4	427.50
$(GUA)_2PtI_6$	531.3	462.39

transition at X is only slightly higher in energy. The valence band is quite flat along the Γ−X line, much like the isotypic Cs_2SnI_6.[12–14]

For $(MA)_2PtI_6$, the valence band is ∼70 meV higher at Γ than at F, while the conduction band minimum occurs at F. This phase then has an indirect bandgap, but the direct transition at F is only slightly higher in energy.

For $(FA)_2PtI_6$, the conduction band is ∼30 meV lower at D than at Γ. The valence band is ∼25 meV higher at Γ than at X, and ∼25 meV higher at Γ than at X. Accordingly, the band gap is indirect, but direct transitions at both Γ and D are only slightly higher in energy.

For $(GUA)_2PtI_6$, the conduction band is nearly degenerate in energy (<10 meV difference) at the M, K, and L points, with the energy at M being the lowest by a slight margin. In contrast, all other local maxima of the valence band are 10s of meV lower in energy than the valence band maximum at Γ. Once again, the bandgap is indirect, but direct transitions at K and L are only somewhat higher in energy.

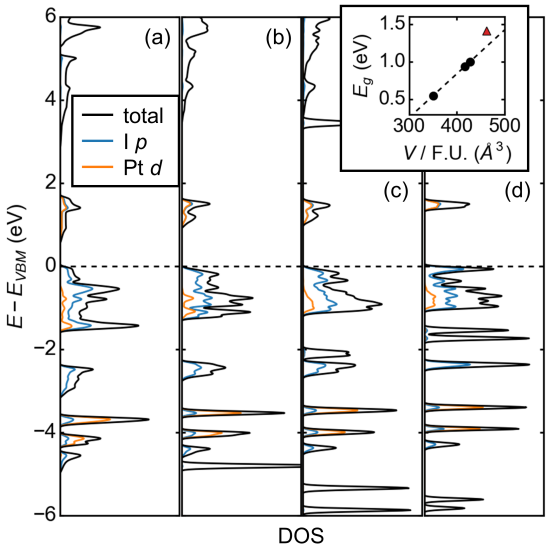

Figure S9: Electronic densities of states (GGA-PBE) for A_2PtI_6 phases, including orbital projections of the I *p* and Pt *d* states. Energies are referenced to the valence band maximum for each phase. Inset: The calculated bandgap is correlated with cell volume for the A = (NH_4), MA, and FA phases (•), which are increasingly distorted versions of the same anti-fluorite structure type. The transition to a different $[PtI_6]^{2-}$ packing arrangement for A = GA (△) widens the bandgap relative to this trend.

The electronic densities of states calculated for the A_2PtI_6 phases, as well as the correlation between bandgap and unit cell volume, are presented in Figure S9. Tracking the position of the localized I *s* states (not shown, ∼12 eV below the VBM) relative to the VBM suggests the VBM drops relative to the vacuum with increasing countercation size (and increasing bandgap). In essence, the band widths are reduced while the band centers remain nearly constant, as expected for phases with somewhat ionic Pt–I bonding and varying degrees of intermolecular I–I contact. For the distorted VHDP ammonium, methylammonium, and formamidinium phases, there is a very strong correlation between bandgap and cell volume (Figure S9 inset), while the different anion packing of the guanidinium phase results in a larger bandgap than expected from this trend.

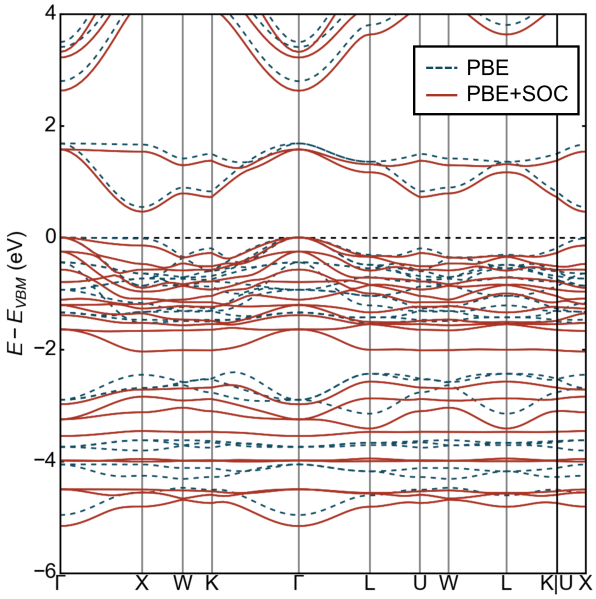

Figure S10: Comparison of PBE to PBE+SOC calculations for $(NH_4)_2PtI_6$.

A calculation was performed on $(NH_4)_2PtI_6$ with both PBE and PBE+SOC, which indicated that the effect of spin-orbit coupling is modest (Figure S10).

Thermogravimetric Analysis (TGA)

Thermogravimetric analysis, presented in Figures S11 - S14, show similar degradation temperatures for each member of the A_2PtI_6 series.

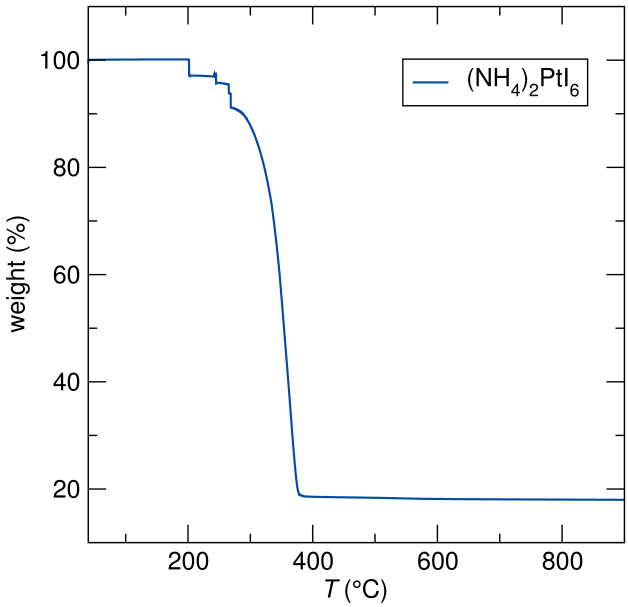

Figure S11: TGA data for $(NH_4)_2PtI_6$ from room temperature to 900°C.

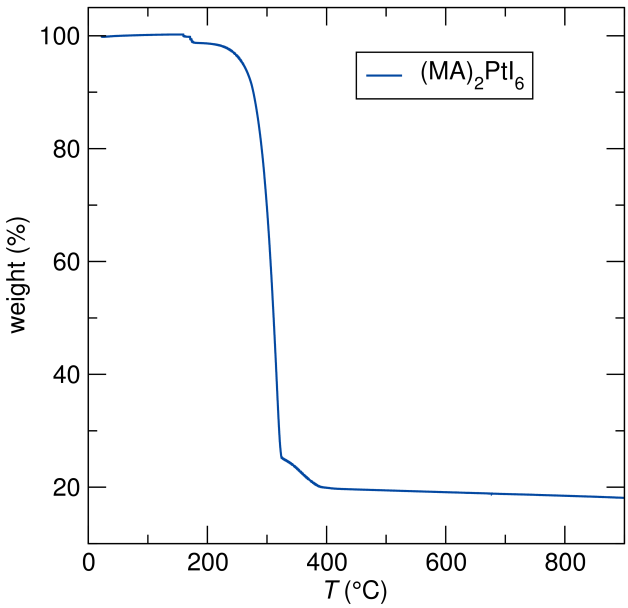

Figure S12: TGA data for $(MA)_2PtI_6$ from room temperature to 900°C.

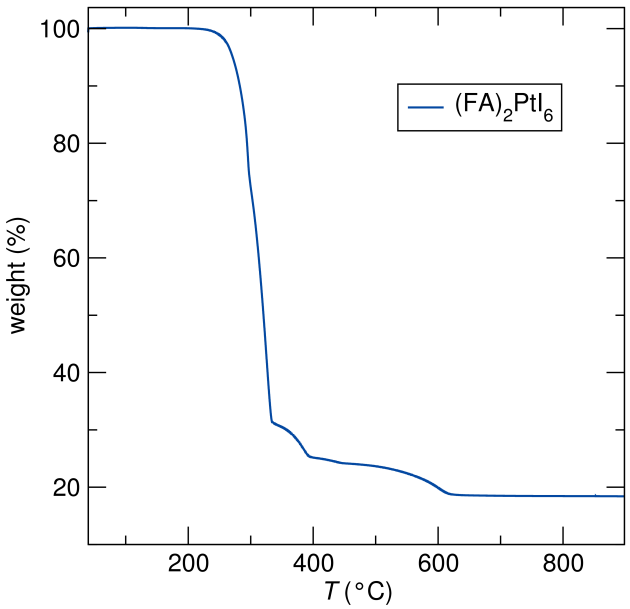

Figure S13: TGA data for $(FA)_2PtI_6$ from room temperature to 900°C.

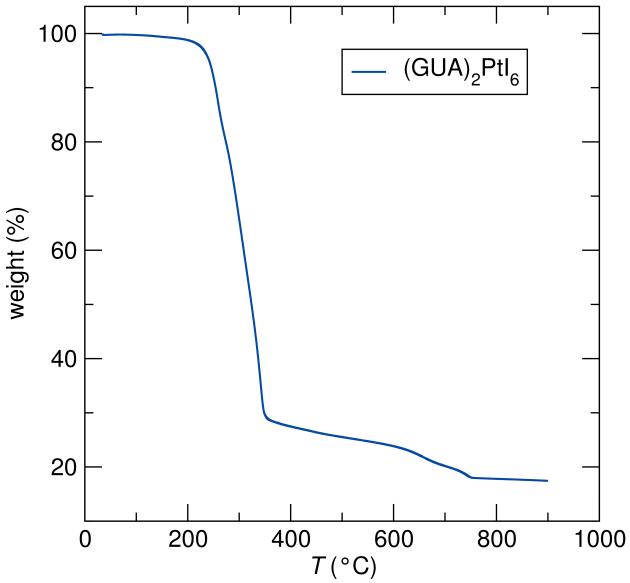

Figure S14: TGA data for $(GUA)_2PtI_6$ from room temperature to 900°C.

Differential Scanning Calorimetry (DSC)

Differential scanning calorimetry of the A_2PtI_6 is presented in Figures S15 - S18.

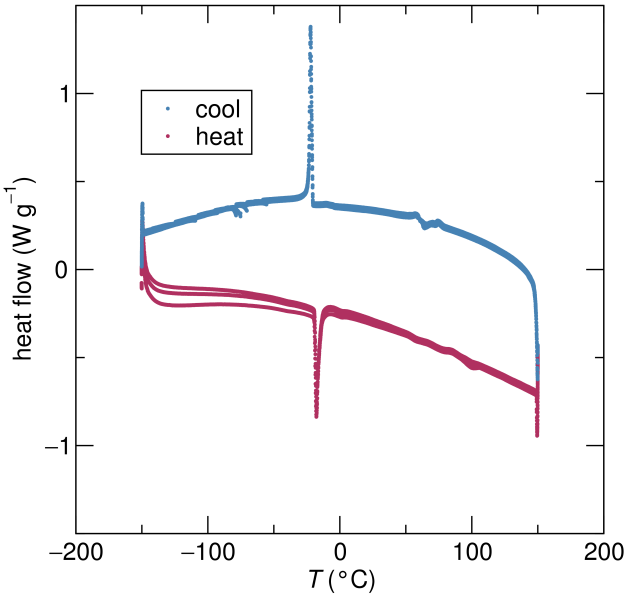

Figure S15: DSC data for $(NH_4)_2PtI_6$ between −150 °C and 150 °C. A first order phase transition can be seen at −20°C.

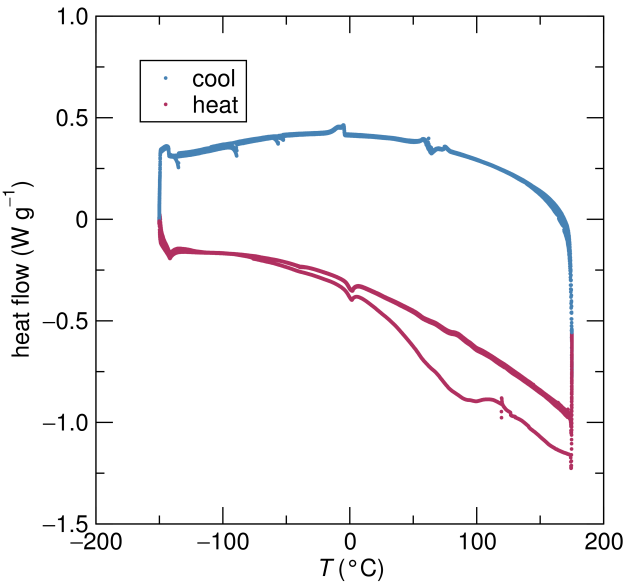

Figure S16: DSC data for $(MA)_2PtI_6$ between −150 °C and 175 °C. No first order phase transition is observed.

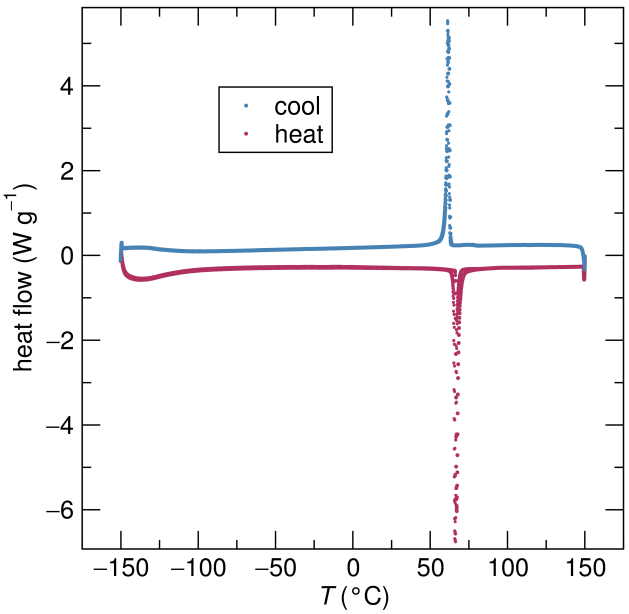

Figure S17: TGA data for $(FA)_2PtI_6$ between −150 °C and 150 °C. A first order phase transition is observed near 63°C.

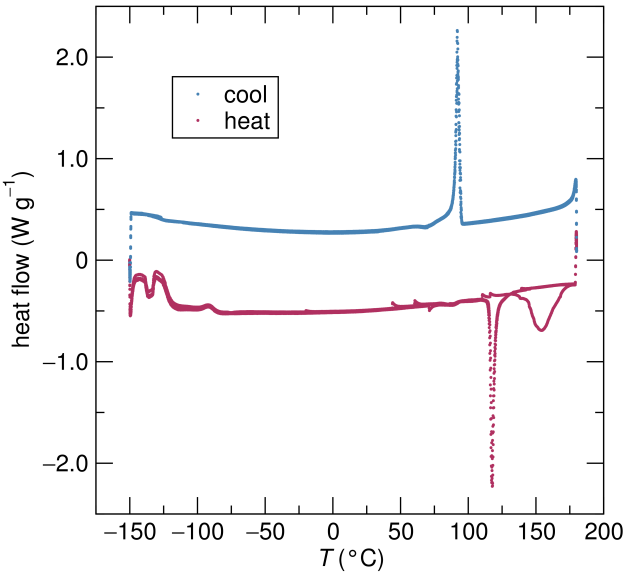

Figure S18: TGA data for $(GUA)_2PtI_6$ between −150 °C and 175 °C. There is a second order phase transition near 100°C associated with increased molecular motion of the guanidinium cation.

References

(1) Ewing, P. J.; Pauling, L. XIII. The Crystal Structure of Potassium Chloroplatinate. *Z. Kristallogr.* **1928**, *68*, 223–230.

(2) Williams, R. J.; Dillin, D. R.; Milligan, W. O. Structure refinement of potassium chloroplatinate by powder and single-crystal methods. *Acta Crystallogr. Sect. B-Struct. Sci.* **1973**, *29*, 1369–1372.

(3) A. Glazer. The classification of tilted octahedra in perovskites. *Acta Crystallogr. Sect. B-Struct. Sci.* **1972**, *28*, 3384–3392.

(4) Kume, Y.; Ikeda, R.; Nakamura, D. Structural Phase Transition in Various Methylammonium Hexahalometallates(IV) as Studied by the NQR of Halogens. *J. Magn. Reson.* **1979**, *33*, 331–344.

(5) Nakamura, D. Nuclear Quadrupole Resonance Studies of Structural and Magnetic Phase Transitions. *J. Mol. Struct.* **1983**, *111*, 341–356.

(6) Larson, A. C.; Von Dreele, R. B. "General Structure Analysis System (GSAS)", Los Alamos National Laboratory Report LAUR, **2000**, 86–748

(7) Toby, B. H. *EXPGUI*, a Graphical User Interface for GSAS. *Appl. Cryst.* **2001**, *34*, 210–213.

(8) Evans, H.A.; Schueller, E.C.; Smock, S.R.; Wu, G.; Seshadri, R.; Wudl, F. Perovskite-Related Hybrid Noble Metal Iodides: Formamidinium Platinum Iodide $[(FA)_2Pt^{IV}I_6]$ and Mixed-Valence Methylammonium Gold Iodide $[(MA)_2Au^{I}Au^{III}I_6]$. *Inorg. Chim. Acta* **2017**, *468*, 280–284.

(9) Ishida. H.; Kashino, S. Bis(dimethylammonium) Hexachlorotellurate(IV). *Acta Cryst.* **1998**, *C54*, 1811–1813.

(10) Ghozlen, M. H. B.; Daoud, A. Dimethylammonium Hexaehlorostannate(IV). *Acta Cryst.* **1981**, *B37*, 1415–1416.

(11) Ishida, H.; Furukawa, Y.; Kashino, S. Bis(guanidinium) hexachlorostannate(IV). *Acta Cryst.* **1999**, *55*, 1995–1997.

(12) Lee, B.; Stoumpos, C. C.; Zhou, N.; Hao, F.; Malliakas, C.; Yeh, C.-Y.; Marks, T. J.; Kanatzidis, M. G.; Chang, R. P. H. Air-Stable Molecular Semiconducting Iodosalts for Solar Cell Applications: Cs_2SnI_6 as a Hole Conductor. *J. Am. Chem. Soc.* **2014**, *136*, 15379–15385.

(13) Maughan, A. E.; Ganose, A. M.; Bordelon, M. M.; Miller, E. M.; Scanlon, D. O.; Neilson, J. R. Defect Tolerance to Intolerance in the Vacancy-Ordered Double Perovskite Semiconductors Cs_2SnI_6 and Cs_2TeI_6. *J. Am. Chem. Soc.* **2017**, *138*, 8453–8464.

(14) Saparov, B.; Sun, J-P.; Meng, W.; Xiao, Z.; Duan, H-S.; Gunawan, O.; Shin, D.; Hill, I. G.; Yan, Y.; Mitzi, D. B. Thin-Film Deposition and Characterization of a Sn-Deficient Perovskite Derivative Cs_2SnI_6. *Chem. Mater.* **2016**, *28*, 2315–2322.